IAMPS

7th International Workshop on Image Analysis Methods for the Plant Sciences

July 4, 2019

7th International Workshop on Image Analysis Methods for the Plant Sciences

Lyon, France

Welcome to IAMPS 2019.

The International Workshop on Image Analysis Methods for the Plant Sciences (IAMPS) intend to bring together scientists interested in the development of methods and tools for image analysis dedicated or adapted for plants. It aims to review the image analysis methods and approaches currently being used and developed, and identify generic image analysis challenges arising from Plant Sciences. It is a forum to facilitate knowledge exchange and collaboration within the community.

After six successful editions in Nottingham, Aberystwyth, Louvain la Neuve, Angers, and Nottingham, the 2019 edition of IAMPS is organized by researchers from the LIRIS laboratory at Université Lumière Lyon2, in France.

This year, we extend the conference to the discipline of robotics, thus broadening its scope for future years. On the one hand, the agricultural robotics field is developing more and more to, for example, help farmers by creating logistical assistance robots. These are "mule" carrier-follower robots, *i.e.* cobots, that follow farmers in the field to carry load (equipment, crops) at his/her place. They also aim to help the farmer take decisions by collecting data, such as crop mapping to define the volume of vegetation to be processed or the type of weed before spraying to reduce the amount of pesticides/fungicides to be used. Automatic image processing tools are increasingly used in this context with various types of imagery ranging from "simple" RGB photos to hyperspectral cameras images embedded on drones or tractors.
On the other hand, some robotics researchers are also interested in developing new generations of robots with a lower environmental impact (in terms of greenhouse gas emissions, for example) than current robots. In this context, the proposed prototypes can be manufactured with bio-sourced materials, such as wood. In summary, plant sciences can guide the confection of robot architectures.

This year spotlights talks, posters and attendees from France, United Kingdom, China, Australia, Japan, Germany, *etc.* working in academia, industry or both.

We would like to thank the Université Lumière Lyon 2 for supporting us and all the members of the LIRIS-Lyon 2 for their help on the conference organization.

General chairs
L. Tougne - LIRIS
C. Crispim Junior - LIRIS

7th International Workshop on Image Analysis Methods in the Plant Sciences

Legend

Conference venue

Lunch

Tram T2

Meeting point for Social activities

University of Lyon 2 – Campus Porte des Alpes

IAMPS

Social events

- Social diner on Thursday July the 4th
  https://www.lesbateauxlyonnais.com/croisiere-restaurant-lyon/diner

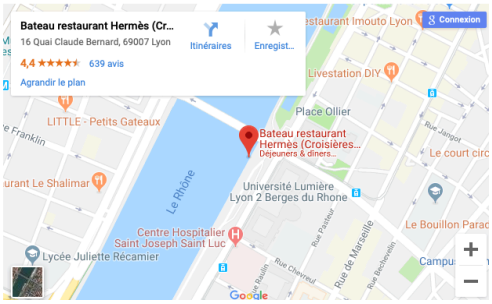

Starting point at “Parilly - Université” (TRAM T2) at 19:30.

- Visit to Lyon old town on Friday, July the 5th.

http://www.lyontraboules.net

Starting point at “Parilly - Université” (TRAM T2) at 15:15 (metro Vieux Lyon – 16:00).

7th IAMPS 2019, 4-5 July 2019, Lyon

International Workshop on Image Analysis Methods for the Plant Sciences

Program

Thursday July the 4th		Friday July the 5th	
9H	Reception/registration		
9H30-10H	Welcome to Lyon 2 - A few words from the organizers	9H00-10H	Keynote 2 : R. Lenain
10H-11H	Keynote 1 : S. Briot	10H00-10H15	Coffee Break
11H-11H15	Coffee Break	10H15-12H45	Oral session 3
11H15-12H45	Oral session 1	12H45-14H	Lunch at the university restaurant
12H45-14H30	Lunch at the university restaurant	14H-15H	Poster session 2
14H30-16H30	Oral session 2	15H-18H	Social Event : Visit of Lyon old town
16H30-16H45	Coffee Break		
16H45-18H00	Poster session 1		
19H30	Diner downtown		

7th IAMPS 2019, 4-5 July 2019, Lyon

International Workshop on Image Analysis Methods for the Plant Sciences

Details of oral sessions

Oral session 1	11H30	**Development of image processing methods for detection and localization of sugar beet leaves in crops for robotic phenotyping operations**
		Bernard Benet and Roland Lenain
	12H	**Toward a procedural fruit tree rendering framework for image analysis**
		Thomas Duboudin, Maxime Petit, and Liming Chen
	12H30	**Estimation of sugar beet resistance to Cercopora Leaf Spot disease using UAV multispectral imagery**
		Sylvain Jay, Alexis Comar, Rafael Benicio, Nicolas Henry, Marie Weiss and Frédéric Baret
Oral session 2	14H30	**Quantifying cell polarities in confocal images using 3D wall meshes**
		Guillaume Cerutti, Carlos Galvan-Ampudia, Jonathan Legrand, Christophe Godin, and Teva Vernoux
	15H	**Statistical multi-scale atlasing of leaf morphogenesis**
		F. Selka, J. Burguet, E. Biot, T. Blein, P. Laufs, and P. Andrey
	15H30	**Statistical integration of image collection for modelling maize stem histology**
		David Legland, Fabienne Guillon, and Marie-Françoise Devaux
	16H	**Accurate dating of organs during growth can unmask invariant developmental patterns: illustration with plant leaf morphogenesis**
		Mohamed Oughou, Eric Biot, Nicolas Arnaud, Aude Maugarny-Calès, Philippe Andrey, Patrick Laufs, and Jasmine Burguet
Oral session 3	10H15	**Green plant segmentation in hyperspectral images using SVM and hyper hue**
		Huajian Liu, Brooke Bruning, Bettina Berger, Trevor Garnett
	10H45	**Evaluation of the Data Distillation strategy for a better generalization of convolutional neural networks in plant phenotyping. A study case onwheat ears detection**
		Etienne David, Raul Lopez-Lozano, Simon Madec, Benoit De Solan and Frédéric Baret
	11H15	**Ripe and unripe raspberry segmentation using u-nets**
		Dominic Williams, Avril Britten, Alison Karley, Susan McCallum and Julie Graham
	11H45	**Combining Computer Vision and Deep Learning for High-Throughput Aerial Phenotypic Analysis in Wheat Pre-Breeding**
		Alan Bauer, Joshua Ball, Joshua Colmer, Simon Orford, Simon Griffiths, Ji Zhou
	12H15	**The P2S2 segmentation dataset: annoted in-field multi-crop RGB images acquired under various conditions**
		Simon Madec, Kamran Ifran, Etienne David, Kaaviya Velumani, Gaetan Daubige, Jeremy Labrosse, Wei Guo, Marie Weiss, Frederic Baret

7th IAMPS 2019, 4-5 July 2019, Lyon

International Workshop on Image Analysis Methods for the Plant Sciences

Details of poster session 1

Poster session 1	**Imagebased phenotyping for wheat vitality**
	Andreas Honecker, Henrik Schumann Diana Becirevic, Lasse Klingbeil, Kai Volland, Steffi Forberig, Hinrich Pau lsen, Heiner Kuhlmann and Jens Léon
	Measurement Method of Leaf Morphology Based on Point Cloud Data
	Chunying Wang, Baohua Liu, Xiang Li and Ping Liu
	Revisiting SIFT for plant foliage in RGB images acquired on a turntable
	Helin DUTAGACI, Etienne BELIN and David ROUSSEAU
	Shape modeling of wheat grain through its development
	Thang Duong Quoc Le, Christine Girousse, David Legland and Anne-Laure Chateigner-Boutin
	Estimation of Leaf Color and Angle based on UAV-Captured Leaf-Scale Images for Indicator of Plant Growth
	Kuniaki Uto, Mauro Dalla Mura, Jocelyn Chanussot, and Koichi Shinoda
	Development of image processing methods for detection and localization of sugar beet leaves in crops for robotic phenotyping operations
	Bernard Benet and Roland Lenain
	Toward a procedural fruit tree rendering framework for image analysis
	Thomas Duboudin, Maxime Petit, and Liming Chen
	Estimation of sugar beet resistance to Cercopora Leaf Spot disease using UAV multispectral imagery
	Sylvain Jay, Alexis Comar, Rafael Benicio, Nicolas Henry, Marie Weiss and Frédéric Baret
	Quantifying cell polarities in confocal images using 3D wall meshes
	Guillaume Cerutti, Carlos Galvan-Ampudia, Jonathan Legrand, Christophe Godin, and Teva Vernoux
	Statistical multi-scale atlasing of leaf morphogenesis
	F. Selka, J. Burguet, E. Biot, T. Blein, P. Laufs, and P. Andrey
	Statistical integration of image collection for modelling maize stem histology
	David Legland, Fabienne Guillon, and Marie-Françoise Devaux
	Accurate dating of organs during growth can unmask invariant developmental patterns: illustration with plant leaf morphogenesis
	Mohamed Oughou, Eric Biot, Nicolas Arnaud, Aude Maugarny-Calès, Philippe Andrey, Patrick Laufs, and Jasmine Burguet

7th IAMPS 2019, 4-5 July 2019, Lyon

International Workshop on Image Analysis Methods for the Plant Sciences

Details of poster session 2

Poster session 2	**Daily high resolution RGB images allow accurate dating of heading stage in wheat crops**
	Kaaviya Velumani, Simon Madec, Jeremy Labrosse, Jocelyn Gillet, Raul Lopez Lozano, Benoit de Solan, Frederic Baret
	Phenomobile: a fully automatic robot for high-throughput field phenotyping of a large range of crops with active measurements
	Frédéric Baret, Benoit de Solan, Samuel Thomas, Philippe Burger, Shouyang Liu, Alexis Comar, Christophe Rousset, Robin Vanhove, Romain Regnier, Jerome Terreni and Laurent Combe
	Hierarchical Structure of the veins of the trees leaves
	Aurélie Leborgne, Julien Mille, and Laure Tougne
	A strategy for multimodal canopy images registration
	Clément Douarre, Carlos F. Crispim-Junior, Anthony Gelibert, Laure Tougne, and David Rousseau
	Toward an automatic Bean Rust disease quantification platform using hyperspectral sensing and Deep Learning
	Anthony Gelibert, Aurélie Thébault, Laurent Descroix, Erica Manesso, Catherine Sirven
	Green plant segmentation in hyperspectral images using SVM and hyper hue
	Huajian Liu, Brooke Bruning, Bettina Berger, Trevor Garnett
	Evaluation of the Data Distillation strategy for a better generalization of convolutional neural networks in plant phenotyping. A study case onwheat ears detection
	Etienne David, Raul Lopez-Lozano, Simon Madec, Benoit De Solan and Frédéric Baret
	Ripe and unripe raspberry segmentation using u-nets
	Dominic Williams, Avril Britten, Alison Karley, Susan McCallum and Julie Graham
	Combining Computer Vision and Deep Learning for High-Throughput Aerial Phenotypic Analysis in Wheat Pre-Breeding
	Alan Bauer, Joshua Ball, Joshua Colmer, Simon Orford, Simon Griffiths, Ji Zhou
	The P2S2 segmentation dataset: annoted in-field multi-crop RGB images acquired under various conditions
	Simon Madec, Kamran Ifran, Etienne David, Kaaviya Velumani, Gaetan Daubige, Jeremy Labrosse, Wei Guo, Marie Weiss, Frederic Baret

Invited speaker: S. Briot (LS2N)

Dr. Sébastien Briot received the PhD degree from the National Institute of Applied Sciences (INSA) of Rennes (France) in 2007. He worked at the Ecole de Technologie Supérieure of Montreal (Canada) as a postdoctorate fellow in 2007-2008. He was recruited at CNRS in 2009 and he is currently working as CNRS researcher in the Laboratory of Digital Sciences of Nantes (LS2N, France). Since 2017, he is the head of the ARMEN research team at LS2N.

His research fields concern the design optimization of robots and the analysis of their dynamic performance. He contributed to the eco-sustainable design of robots by using plant-based bio-sourced materials for robot design purpose and also studied the impact of sensor-based controllers on the robot performance.

Dr. Briot received the Award of the Best Ph.D. Thesis in Robotics from the French CNRS Research Group in Robotics for year 2007. In 2011, he received two other awards: the Award for the Best Young Researcher from the French Region Bretagne and the Award for the Best Young Researcher from the French Section of the American Society of Mechanical Engineering (SF-ASME).

Robotics for Plants, Plants for Robotics

Robotics is more and more essential in many aspects of our human life, but also in plant life. Many robots are currently being developed to take care of plants: for example, to monitor their well-being, to propose new strategies to reduce the use of pesticides in agriculture, for crop phenotyping, for automatic harvesting. The first part of this presentation will present some relevant works related to the use of robots for plant monitoring and cultivation with some focus on image processing approaches used in these works.

Robotics also takes inspiration from plants at different levels:

- Bio-inpiration, i.e. the translation of fundamental biological principles into engineering design rules so that robot performs like a natural systems: e.g. artificially growing robots, robots behaving like plant roots for soil exploration and monitoring, robots performing artificial photosynthesis in order to produce their own energy,
- Bio-hybridation, i.e. the direct use of (living) materials in order to design synthetic machines: e.g. plant bio-hybrid robots designed for modifying architectural ambiances,
- Ecosustainability, i.e. the use of plant-based bio-sourced materials in order to lower robotics environmental impact: e.g. industrial robots designed in wood, in plant composites.

In the second part of this talk, we will review main works in these fields and disclose their key issues, goals and interests, with a special focus on the use of plants for eco-design purpose at LS2N.

Invited speaker: R. Lenain (IRSTEA)

Roland Lenain is currently research director at Irstea (National Research Centre for Environment and Agriculture) in the unit TSCF (Technology and Information Systems) at Clermont-Ferrand (France). He received a mechanical engineer degree from french institute for advanced mechanics in 2002. He obtained the same year a master degree in mechanical and civil engineering. He defended is PhD in 2005 on the topis of automatic guidance of off-road mobile robots, at University Blaise Pascal (Clermont-Ferrand, France). After completing a post doctoral position in the department of Automatic Control in Lund University (sweden), he joined Irstea in 2006. He supervised several projects and thesis on topic of mobile robot control in harsh environment. He obtained the capability to conduct research in 2011, and currently lead the team Romea (Robotic and Mobility for Environment and Agriculture). He is also in charge of the theme terestrial mobile robotics of the National Research Group on Robotics. His research activities, focused on adaptive and predictive control of mobile robots in the context of natural environment, are deeply applied in the field of agricultural robots.

Robotics in agriculture, a new vision

The challenge of reducing environmental impacts of human activities, while preserving production level and human safety, resuires the development of new tools for agriculture. The reduction of chemical products indeed leads to the use of alternative solutions, implying more frequent treatments, and plant monitoring. Such manual operations then arises as time consuming and harmful. As a result, the use of robots then appears as a promising solution for both field surveillance as well as treatments. Nevertheless, the motion control of robots in off-road contexts is still challenging, because of the diversity and uncertainty of conditions and missions to be done. The talk will give an overview of the robotics in agriculture. From actual robots currently marketed to prototypes and new concepts, different aspects linked to the autonomy in off-road conditions will be described, such as sensors and perception systems (including vision), control purpose, as well as decision making. Throught many examples, the talk will give the current state of the art, the challenges and the prospects of agricultural robots, and their potential interests for social needs.

Development of image processing methods for detection and localization of sugar beet leaves in crops for robotic phenotyping operations

Bernard Benet and Roland Lenain

Université Clermont Auvergne, Irstea, UR TSCF, Centre de Clermont-Ferrand, F-63178 Aubière, France

Abstract

For phenotyping operations, artificial vision devices operating in visible or hyperspectral color fields are used to perform geometric and colorimetric measurements. A robotic platform with a manipulator arm has been developed to detect diseases on sugar beet crops, during different growing stages. Image processing algorithms have been developed to separate plants, to localize leaves of each one. From this information, active perception operations were applied to put the camera located at the end of the effector of the robot, at the desired locations above the beet leaves. A new vision algorithm was then applied to detect sick areas on leaves.

Keywords: Image processing, Machine Learning, Robotics, Manipulator arm, Phenotyping

1 Introduction

For sugar beet plants, the most important diseases which can affect the crops, during the growth process, are Oidium and Cercosporiose contamination. It is necessary to detect as soon as possible these diseases, in order to limit their development and propagation in the cultures. In recent years, the use of new technologies has become widespread in agriculture, through precision farming, with the aim of improving agricultural operations. The evolution of increasingly sophisticated perception sensors has enabled the development of high performance autonomous navigation systems, which can, in particular, perform agricultural tasks of crop monitoring, and measurements for different types of plants, while limiting human intervention, relatively restrictive. An important point of growing interest for the agricultural community is the protection of crops against a variety of factors that lead to reduced yields, such as diseases, that can affect plants during the growth process. There are several diseases that affect plants with the potential to cause devastating economic, social and ecological losses. In this context, diagnosing diseases in an accurate and quick way is of utmost importance. Vision devices are currently used to detect some diseases, which can be seen in the visible or invisible lighting spectrum. A large amount of information on the subject can be found in the papers by [1,2,3]. Fungal diseases have recently led to losses in world production, especially for sugar beet, wheat or maize. Article in [4] contains a state of the art of disease detection from different types of sensors (RGB, thermal, hyperspectral ...). The improvement of disease detection by automatic objective tools has become a major concern for agricultural producers. In this paper, we will focus on the development of phenotyping tools and techniques to realize automatically by artificial vision, geometric and colorimetric measurements on sugar beet plants, for three operations: plant detection, leaf separation and disease detection. In [5], a comparison of leaf detection algorithms was presented during the Leaf Segmentation Challenge in 2014. For disease detection, the objective was to develop an autonomous robotic system allowing putting a camera at the desired location for each leaf, taking into account various camera positions and orientations, using active perception, in order to acquire images with a high accuracy.

2 Material and Methods

A robotic platform composed by a motorized linear axis which carried a manipulator arm with six degrees of freedom (UR5 Universal Robot) was developed for disease detection. At the end of this arm, a vision sensor (color or hyperspectral camera) was embedded to acquire and process images on sugar beet crops, with the possibility to acquire images with various heights and orientations. Figure 1 below shows Bettybot robot used with a RGB camera. First works achieved in image processing with this robot are presented in [6].

Bettybot robot

Sugar beet images

Figure 1: Bettybot robot with RGB camera for phenotyping

Image processing algorithms were developed and applied to achieve three successive tasks: plant detection and separation, leaf localization for each plant and disease detection.

3 Plant detection

The image processing method used to detect and separate plants in a crop line was composed by several successive image processing functions: RGB to HSV conversion, Filtering in H component to extract leaf green color, Canny method in V component to recover ribs and stems, Line detection with HoughLine method, Cross point detection between extended lines and finaly Morphological operations to obtain the center of each plant. A machine learning operation was added to the image processing functions, in order to improve the sugar beet center detection. For this operation, a learning stage was achieved before, considering three object classes (background images, leaf images and images containing a plant center), using inception-V3 neural network, Tensorflow tool and a 'retrain' method to obtain the neural network for our application, using our image database which contained about 50 images for each class. In Figure 2 some plant center detection results (object class and score (in red color)) are presented.

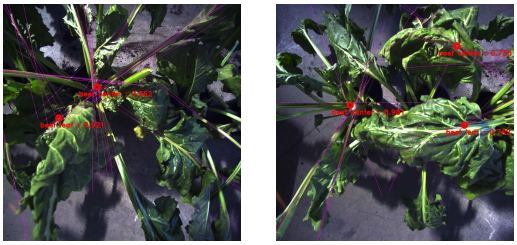

Figure 2: Sugar beet plant center detection

4 Leaf separation

To detect the leaves for each plant (gravity center (in red color) and main inertial axis (in white color)), after detection of each plant, a new algorithm was applied, with the following functions (Figure 3): RGB to HSV conversion, Edge detection with Sobel method, Filtering in H component using Sobel method results, DistanceTransform function and finaly Watershed algorithm to find leaves.

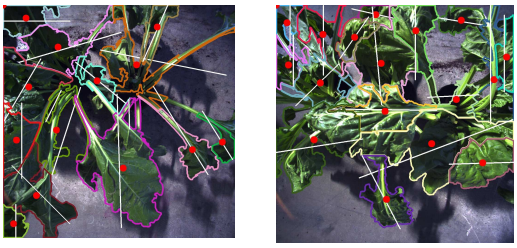

Figure 3: Sugar beet leaf detection

5 Disease detection

For detecting main diseases which affect sugar beet plants, an image processing method containing filtering operations in HSV color space and morphologic functions were applied.

Figure 4 presents disease detection results: Oidium and Cercosporiose respectively in blue and red color.

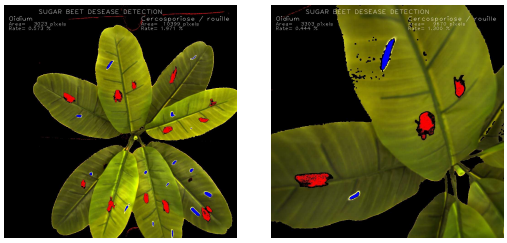

Figure 4: Disease detection

6 Conclusion - Discussion

Experimentations with the phenotyping robot were achieved inside a laboratory to test and validate the images processing algorithms and active perception methods to put the camera at desired positions from detected leaves, for disease detection. The objective was to find parameters for image processing operations to obtain the best results as possible for plant center detection and leaf separation. The optimal sets of parameters permitted to obtain a success rate of 90% for center plant detection with the complementary use of the machine learning operation and a success rate of 80% for leaf separation. In 2019, applications will be achieved with Bettybot robot embedded on a tractor, to study the disease propagation in sugar beet fields, considering different growing stages.

References

[1] Bock, C. H., Poole, G. H., Parker, P. E., and Gottwald, T. R. 2010. Plant disease severity estimated visually, by digital photography and image analysis, and by hyperspectral imaging. Crit. Rev. Plant Sci. 29:59-107, USA.

[2] Mahlein A.K. , Steiner U., Hillnhütter C., Dehne H.W. and Oerke E.C.. Hyperspectral imaging for small-scale analysis of symptoms caused by different sugar beet diseases. Plant Methods2012 8:3, Germany

[3] Sankaran S., Mishra A., Ehsani R., Davi C.. A review of advanced techniques for detecting plant diseases. Computers and Electronics in Agriculture72 (2010) 1–13, USA

[4] Barbedo J.G.A.. Digital image processing techniques for detecting, quantifying and classifying plant diseases. SpringerPlus, 2(1) :1, 2013.

[5] Scharr H., Minervini M., French A.P., Klukas C., Kramer D.M., Liu X., Luengo I., Pape,G J.M.,. Polder, D. Vukadinovic, X. Yin, and S. A. Tsaftaris. Leaf segmentation in plant phenotyping : a collation study. *Machine Vision and Applications*, 27(4) :585–606, May 2016.

[6] Benet, B., Dubos, C., Maupas, F., Malatesta, G., Lenain, R. - Development of autonomous robotic platforms for sugar beet crop phenotyping using artificial vision, AGENG Conference, July 2018, Wageningen, NLD.

Toward a procedural fruit tree rendering framework for image analysis

Thomas Duboudin[1], Maxime Petit[1], and Liming Chen[1]

[1]LIRIS, CNRS UMR 5205, Ecole Centrale de Lyon, France

Abstract

We propose a procedural fruit tree rendering framework, based on Blender and Python scripts allowing to generate quickly labeled dataset (*i.e.* including ground truth semantic segmentation). It is designed to train image analysis deep learning methods (*e.g.* in a robotic fruit harvesting context), where real labeled training datasets are usually scarce and existing synthetic ones are too specialized. Moreover, the framework includes the possibility to introduce parametrized variations in the model (*e.g.* lightning conditions, background), producing a dataset with embedded *Domain Randomization* aspect.

Keywords: Synthetic Fruit Dataset, Harvesting Robotics, Procedural Model, Domain Randomization

1 Introduction and Previous Work

State-of-the-art methods for object recognition and grasping are currently mostly based on deep neural network. Despite tremendous results, these methods require a huge amount of labeled data in order to be trained. This is a major drawback in the field of robotics fruit-harvesting, where existing dataset are usually too small and/or dedicated to a single specie (*e.g.* [1, 2]).

We previously tackled this issue for indoor object grasping robots using a simulated environment and rendering engine [3, 4]. We apply here a similar strategy for fruits harvesting problems by defining a framework capable of generating scenes of fruit trees coupled with procedural scripts controlling parameters (*e.g.* position of the fruits, type of background, lightning condition) to introduce realistic variations for outdoor data[1].

One of the most photo-realistic synthetic dataset of fruit trees is the work of Barth *et al.* [2] for sweet pepper. This come at the price of a huge computational cost (10 min/frame with a 16 core processor) preventing it to be easily extendable in order to produce large dataset for other fruits. In fact, such high degree of photo-realism does not seem to be needed for deep simulated learning [5]. That is why we aim at only an adequate photo-realism with quick rendering and easy-generation method, allowing scientists to create their own fruits or tree dataset according to their precise research interests.

2 Material and Methods

We chose the open-source Blender as the 3D-modelling and rendering software. Every options accessible through the Blender GUI can be reached and modified through a Python API, enabling us to entirely control the simulation with scripts.

The framework can be decomposed in two steps : first the generation of the tree or plant models, then a rendering script.

[1]Source code available at https://github.com/tduboudi/IAMPS2019-Procedural-Fruit-Tree-Rendering-Framework

Figure 1: Samples of synthetic oranges (top) and apples (bottom) with different lightning conditions and rendering qualities.

It mainly contains a animation loop, such as that each time-step is responsible for the rendering of one image (and a semantic segmentation map, corresponding to the ground truth label), different from the previous ones.

Tree models are generated following the rules of Weber and Penn [6] using an existing Blender tree generation add-on, controlled by the Python generation script. It defines a number of parameters such as the branching frequency, the decrease in the radius of trunks and branches, the overall direction of the branches (up or down), the ratio tree height/branches length, *etc*. The fruits and the leafs are randomly and uniformly added upon the naked tree following defined densities.

The camera movements has to be defined in the rendering script, in which position and orientation of the camera should be directly provided at each time-step. We usually use a new random position and orientation at each iteration, such that the camera is globally pointing toward the models (see Fig.2). While it has to be noted that the camera trajectories do not have

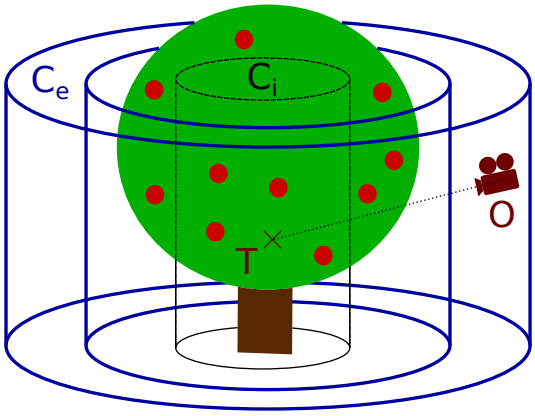

Figure 2: Schema of the camera point of view generation. Camera origin O and target point T are uniformly picked from respectively the hollow external cylinder C_e and the internal cylinder C_i (centered around the model).

to be continuous, we can also create robotic-like continuous trajectories toward branches on a tree. In addition, depth of field and rendering-engine parameters (*e.g.* number of rays for the ray-tracing engine) can be randomly modified within a certain range every time-step.

Background and lightning are also controlled in the rendering script, and can be easily changed every few time-steps to generate diverse images. This is a much needed feature allowing *Domain Randomization*, known to be efficient in reducing the *Reality Gap* encountered when transferring deep neural networks from simulation to the real world [7]. In order to have complex backgrounds we use freely available spherical HDRIs (high-dynamic-range 360° images), which control the lightning and the background objects. The tree models are placed in the center of the HDRIs.

3 Results and Discussion

Overall, the rendering of one pair of images (512x512 pixels, raw and ground truth for semantic segmentation) is fairly quick with ~[10s:30s] with GPU-rendering (NVIDIA GTX 1080). Fig.1 illustrates different possible variations for the scene generation (*e.g.* fruits, light) and the quality of the rendering.

4 Conclusion and Future Work

We designed a framework for semantic segmentation and object recognition field related to robotics fruit harvesting problems. It allows a quick and efficient fruit trees scene generation with parametrized variations, thus producing labelled images embedding a *Domain Randomization* aspect.

We aim to extend our framework to reproduce the variations occurring during the lifetime of the fruits and tree. For instance, an implementation of the fruit senescence and decay [8] unlocks the training of mature fruit picking robot and disease detection systems. We also plan to improve the photo-realism of the simulated image by using a Generative Adversarial Network as in [9], allowing to keep the rendering time needed quite low.

Acknowledgment

This work is supported by the french National Research Agency (ANR), through the ARES labcom (grant ANR 16-LCV2-0012-01) and by the CHIST-ERA EU project "Learn-Real".

References

[1] I. Sa, Z. Ge, F. Dayoub, B. Upcroft, T. Perez, and C. McCool, "Deepfruits: A fruit detection system using deep neural networks," *Sensors*, vol. 16, no. 8, p. 1222, 2016.

[2] R. Barth, J. IJsselmuiden, J. Hemming, and E. J. Van Henten, "Data synthesis methods for semantic segmentation in agriculture: A capsicum annuum dataset," *Computers and electronics in agriculture*, vol. 144, pp. 284–296, 2018.

[3] A. Depierre, E. Dellandréa, and L. Chen, "Jacquard: A large scale dataset for robotic grasp detection," in *2018 IEEE/RSJ Int. Conf. on Intelligent Robots and Systems (IROS)*, 2018, pp. 3511–3516.

[4] M. Petit, A. Depierre, X. Wang, E. Dellandréa, and L. Chen, "Developmental bayesian optimization of black-box with visual similarity-based transfer learning," in *The 9th Joint IEEE Int. Conf. on Development and Learning and on Epigenetic Robotics (ICDL-Epirob)*, 2018.

[5] M. Rahnemoonfar and C. Sheppard, "Deep count: fruit counting based on deep simulated learning," *Sensors*, vol. 17, no. 4, p. 905, 2017.

[6] J. Weber and J. Penn, "Creation and rendering of realistic trees," in *Int. ACM Conf. on Computer graphics and interactive techniques*, 1995, pp. 119–128.

[7] J. Tobin, R. Fong, A. Ray, J. Schneider, W. Zaremba, and P. Abbeel, "Domain randomization for transferring deep neural networks from simulation to the real world," in *IEEE/RSJ Int. Conf. on Intelligent Robots and Systems (IROS)*, 2017, pp. 23–30.

[8] J. T. Kider Jr, S. Raja, and N. I. Badler, "Fruit senescence and decay simulation," in *Computer Graphics Forum*, vol. 30, no. 2, 2011, pp. 257–266.

[9] R. Barth, J. Hemming, and E. J. van Henten, "Improved part segmentation performance by optimising realism of synthetic images using cycle generative adversarial networks," *arXiv preprint arXiv:1803.06301*, 2018.

Estimation of sugar beet resistance to Cercopora Leaf Spot disease using UAV multispectral imagery

Sylvain Jay[1] , Alexis Comar[2] , Rafael Benicio[2], Nicolas Henry[3], Marie Weiss[1] and Frédéric Baret[1]

[1] INRA UMR 114 EMMAH, UMT CAPTE, Domaine Saint-Paul, Site Agroparc, F-84914 Avignon, France
[2] HIPHEN SAS, 22b rue Charrue, 84000 Avignon, France
[3] Florimond Desprez, 59242 Capelle-en-Pévèle, France

Abstract

Cercospora Leaf Spot (CLS) disease can greatly affect sugar beet yield, thus requiring the selection of resistant cultivars. In this study, we propose a methodology based on UAV multispectral imagery acquired after disease inoculation to estimate sugar beet resistance to CLS. Using a large data set including three years and two sites, we show that exploiting the temporal dynamics of green fraction allows us to predict cultivar resistance with an error of 15 %, without requiring visual scoring. This is promising in the perspective of large field phenotyping experiments, where thousands of microplots have to be compared.

Keywords: Cercospora Leaf Spot, Field phenotyping, Remote Sensing, Sugar beet, UAV.

1 Introduction

Cercospora leaf spot (CLS) caused by the *Cercospora beticola* Sacc. fungus is one of the most damaging foliar diseases for sugar beet (*Beta vulgaris* L.) crops, moderate infestation inducing losses of around 1 t/ha and up to 30% in recoverable sucrose [1]. This fungus causes increasing necrosis, ranging from a few brown spots for the earliest stages to fully necrosed plants for the latest stages. Current solutions to limit CLS influence include the use of fungicides and the selection of resistant cultivars. These solutions require assessing CLS severity along the crop growth, which is usually performed visually by experts. However, this procedure is subjective and time-consuming. On the other hand, the use of optical sensors embedded on unmanned aerial vehicles (UAVs) appears as a promising alternative to reach the required accuracy, reproducibility and throughput. However, despite an increasing demand, there are still few studies focusing on the assessment of cultivar resistance to plant diseases under natural field conditions with a large number of cultivars, as required for field phenotyping experiments.

In this study, we exploit UAV and ground measurements collected over sugar beet microplots to develop a method based on the dynamics of normalized difference vegetation index (NDVI) and green fraction (GF) for assessing resistance to CLS. Data and methods are presented in Section 2. Results are presented and discussed in Section 3, and conclusions are drawn in Section 4.

2 Material and methods

a. Data acquisition

Field experiments were conducted in Castelajoux, France in 2016 (80 microplots) and 2017 (1374 microplots), and in Agen, France in 2018 (1522 microplots). For each year, several cultivars were considered. The microplots were generally submitted to the same modality, i.e., they were inoculated with *Cercospora Beticola* at the beginning of July and no fungicide was applied afterward. For each microplot, CLS disease severity was evaluated visually by an experienced expert 4 to 6 times along the disease development, using a scoring scale ranging from 1 (no CLS spots) to 9 (every leaf is necrosed). The area under the curve was computed by integrating the dynamics of these instantaneous scores over the considered period (in growing degree days), providing the Area under Disease Progress (ADPC) variable [2] used to assess cultivar resistance.

UAV multispectral images of microplots were acquired at 5 to 8 dates after disease inoculation using an AIRPHEN[1] camera sampling the reflected radiation in 450, 530, 570, 675, 730 and 850 nm spectral bands. The image spatial resolution was 0.9 cm in 2016 and 2.3 cm in 2017 and 2018. Multispectral bands were then co-registered, geometrically and radiometrically calibrated as described in [3].

b. Estimation of disease resistance from UAV

The dynamics of NDVI [4] and GF were used to estimate instantaneous disease scores and, in turn, ADPC. Here, GF was estimated by thresholding the VARI [5] index image, as described in [3]. To decrease the influence of variations in canopy structure among microplots of similar disease scores, we compared the results obtained with three dynamics for both NDVI and GF: (i) raw dynamics, (ii) dynamics normalized by the maximum value, and (iii)

[1] http://www.hiphen-plant.com/our-solutions/airphen/

dynamics normalized by the maximum value and values set to 1 before this maximum. These dynamics were finally resampled to the dates of visual scoring, resulting in 480, 5496 and 7610 samples for 2016, 2017 and 2018, resp.. NDVI- and GF-based variables as obtained from the three dynamics were non-linearly related to instantaneous disease scores using Gaussian Process regression. Estimated scores were then integrated to estimate ADPC for every microplot, similarly as for visual scores (Section 2.a). The estimation accuracy was evaluated using a cross-validation process, using two years for calibration (randomly selecting the same number of samples for both years) and the remaining year as an independent validation set, and repeating this procedure three times to use every year for the validation.

3 Results and discussion

When considering raw dynamics, similar results are obtained using NDVI and GF, with root mean square errors of prediction (RMSEP) of about 24 %, 38 % and 10 % for 2016, 2017 and 2018, resp. (Table 1).

Significant improvements are generally observed when normalizing the dynamics by the maximum values. In this case, NDVI performs better for 2016 (RMSEP = 18 %), while GF performs better for 2017 and 2018 (RMSEPs of 24 and 7 %, resp.). Normalization allows us to take into account differences in canopy structure between years that may be due to differences in soil and weather conditions.

For every year, the best results are, however, obtained when exploiting the GF dynamics normalized by its maximum value and with GF values set to 1 before this maximum. This configuration allows us to achieve RMSEPs of 17, 22 and 7 % for 2016, 2017 and 2018, resp., which corresponds to an overall RMSEP of 15 % (Figure 1). Setting the normalized dynamics to 1 before the maximum value allows us to exploit the temporal information and to limit confusions between GF variations due to crop growth (increase in GF until the maximum) and those due to disease development (decrease in GF after the maximum). The superiority of GF compared to NDVI may be due to the differences in soil properties or leaf chlorophyll content across sites. Such differences do not relate to the disease severity, still they affect the NDVI values while keeping the GF values unchanged.

Table 1: RMSE (in %) obtained for the estimation of ADPC with the three dynamics of the two remote-sensing variables considered. For each year, the best results are in bold.

Remote-sensing variable	Dynamics type	2016	2017	2018
NDVI	Raw	24	37	11
	Normalized	18	28	12
	Normalized + 1's	25	24	13
GF	Raw	24	39	10
	Normalized	21	24	**7**
	Normalized + 1's	**17**	**22**	**7**

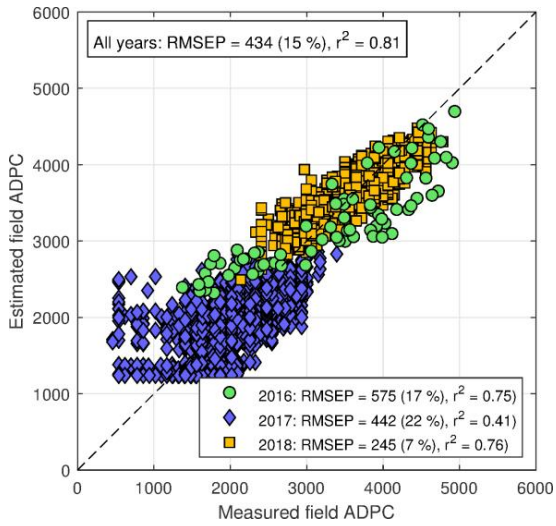

Figure 1: ADPC estimation results obtained with the GF dynamics normalized by the maximum value and with GF values set to 1 before this maximum.

4 Conclusions

In this study, we demonstrate the potential of UAV multispectral imagery to assess sugar beet resistance to CLS disease. An overall ADPC estimation error of 15 % is obtained based on the dynamics of GF. As such methodology does not require subjective and time-consuming field measurements, it offers promising perspectives for field phenotyping experiments.

5 Acknowledgement

This work was supported by the French National Research Agency in the framework of the "Investissements d'avenir" program AKER (ANR-11-BTBR-0007).

References

[1] M. Khan *et al*. Cercospora leaf spot control in Eastern North Dakota and Minnesota in 2000. 2000 Sugarbeet Res. Ext. Rep. ND State Univ, 32: 303-310, 2001.

[2] G. Shaner and R. Finney. The Effect of Nitrogen Fertilization on the Expression of Slow-Mildewing Resistance in Knox Wheat. Phytopathology, 1051-1056, 1977.

[3] S. Jay *et al*. Exploiting the centimeter resolution of UAV multispectral imagery to improve remote-sensing estimates of canopy structure and biochemistry in sugar beet crops. Remote Sens. Environ, in press, 2018.

[4] J.W. Rouse *et al*. Monitoring vegetation systems in the great plains with ERTS. Third Earth Resour. Technol. Satell. Symp., 1:309:317, 1973.

[5] A.A. Gitelson *et al*. Novel algorithms for remote estimation of vegetation fraction. Remote Sens. Environ, 80: 76-87, 2002.

Quantifying cell polarities in confocal images using 3D wall meshes

Guillaume Cerutti[1], Carlos Galvan-Ampudia[1], Jonathan Legrand[1], Christophe Godin[1], and Teva Vernoux[1]

[1]Laboratoire Reproduction et Développement des Plantes, Univ Lyon, ENS de Lyon, UCB Lyon 1, CNRS, INRA, Inria, F-69342, Lyon, France.

Abstract

Polarized transport of signaling molecules, such as the phytohormone auxin, is a core process for the establishment of gradients involved in the patterning of multicellular plant tissues. Cell-to-cell polarity of transport can result from the differential deposition of efflux carriers on the membranes at the interface between cells, as for the pin-formed1 (PIN1) auxin transporter. Quantifying such sub-cellular information in whole organ microscopy images constitutes a real challenge. In this work, we propose a method that computes polarities at the level of cell-to-cell interfaces starting from standard resolution confocal images and using a 3D geometric representation of cell walls. A robust estimation of spatial fluorescence distribution around cell walls allows quantifying polarity with a fair level of confidence, and opens the way for the automated analysis of polar transport at tissue scale.

Keywords: Quantitative Image Analysis, Confocal Microscopy, Triangle Mesh, Polar Transport.

1 Introduction

Cell polarity is a fundamental feature in developmental biology, where symmetry breaking is essential for the formation of patterns in multicellular organisms. In plants, along with anisotropic cell elongation or asymmetric cell division, polarity manifests notably by a preferred directionality in the intercellular flow of signaling molecules. In the preeminent case of auxin, polarized transport, mediated by the PIN efflux carriers, has been shown to play a determinant role in the establishment of early embryo apico-basal axis [1], aerial organ arrangement (phyllotaxis) [6], or leaf adaxial-abaxial axis [7]. It is the localization of such proteins at the plasma membrane on a preferential side of the cell that will increase the export of molecules to neighbor cells in a given direction, and locally orient the flow.

Live-imaging microscopy is used to monitor levels of transporters in a developing tissue, and to assess polarity of transport at cell-level. It is generally admitted that intracellular gradients mark the polarity of a transporter, and without reference for the cell wall position, the visual cue of a crescent shape on one side of a cell in 2D projections is often used to manually estimate cell polarities. However, in confocal images of transporters where the 0.1-0.2μm resolution exceeds cell wall thickness, it is impossible to visually assert which cell hosts the fluorescence, and ultimately to determine polarity. Recent works begin to rely on co-imaging to estimate the relative position of transporters and cell wall intensity peaks in 2D along user-specified lines [7].

Here, we propose a fully automated method to estimate polarities of transporters in confocal images using a cell wall marker reference and going beyond voxel resolution through the use of geometric representations detached from the image grid.

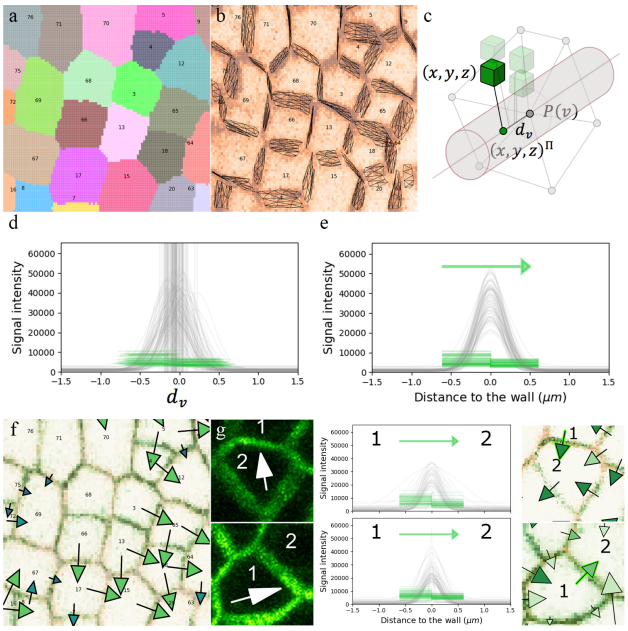

Figure 1: Wall-level quantification of transport polarity: 3D segmented image slice (a), projected wall meshes (b), locally orthogonal cylinder placed at each vertex of the wall and voxel projection (c), precise location of the cell wall intensity mode (d), left and right estimation of transporter levels and statistical polarity decision (e), tissue level polarity vectors (f), decorrelation between visual interpretation of intensity crescents and quantitative polarity estimation (g).

2 Wall polarity quantification

Our starting point consists of a 3D segmented image of multicellular tissue (Figure 1a), typically obtained by applying an automatic seeded watershed algorithm to a confocal stack of membrane or cell wall marker, where seeds can be detected as regional minima of signal [3]. Our polarity estimation algorithm has two steps : the extraction of cell walls as 3D triangular meshes, and the estimation for each wall of a polarity vector through the analysis of the local fluorescence distribution.

We use smooth triangular meshes to represent accurately the cell walls and limit the sensitivity to noisy segmentation and to image resolution. To obtain such meshes, we apply the Marching Cubes algorithm [5] to the binary image corresponding to each labelled cell region in the segmented image, and keep the common vertices for each pair of neighbor cells, using the triangulation of either of the two to define mesh elements. Those meshes undergo a phase of triangle decimation [4] and isotropic remeshing [2] to obtain a regular surface (Figure 1b). On the triangular mesh, we estimate the normal vectors at each vertex and the area of each triangle that allows us to estimate the total area of the interface between the two cells.

We consider that the transporter polarity vector of a given cell interface, i.e. whether the efflux carriers orient the flow of molecules towards one cell or the other, is given by the differential of concentration of transporters between the plasma membranes. We access this information through the difference of fluorescence intensity in the image on either side of the cell wall marked by the wall-marker intensity around each mesh.

We generate a set of 3D cylinders, placed at each vertex in the direction of the normal, in which we will sample the image signals. We position the image voxels lying inside this cylinder on an 1-dimensional axis by assigning them the signed abscissa d_v of their orthogonal projection on the main axis (Figure 1c). The position $d_v = 0$ (corresponding to the mesh vertex supporting the cylinder) might actually have shifted from the actual cell wall in the consecutive processing steps (segmentation artifacts, meshing simplifications, smoothing approximations). To account for this, we locate precisely the abscissa d_0 of the mode in the 1D wall-marker image intensity distribution by the least-squares fitting of a Gaussian-shaped function. Then, transporter levels are quantified on either side of this reference, up to a distance d_{max}, by computing the average voxel intensity within the two sub-cylinders (Figure 1d).

By performing this two-sided estimation on every cylinder defined by the wall triangular mesh, we end up with two parallel transporter signal distributions. We test statistically whether these distributions can be seen as significantly different by an ANOVA test, and decide that a polarity exists when the test gives a p-value < 0.05 (Figure 1e). In such case the polarity vector is given by the difference between the medians of the two distributions multiplied by the normal vector to the wall, otherwise it is null (Figure 1f).

3 Results & Discussion

We have applied our method to root images expressing fluorescent PIN2 and with stained cell walls using propidium iodide (PI). It is known that, in root epidermal cells, auxin transport is polarized shootward, and our method retrieves this expected polarity in all cells. We also studied the influence of spatial resolution and showed similar PIN1 polarities between shoot apical meristem (SAM) tissues imaged at 0.1μm and 0.2μm resolutions. Finally, a study on 16 SAM images reveals highly preserved patterns of PIN1 polarities, indicating that our method provides consistently reliable results at tissue scale.

Additionally, this 3D reconstruction of PIN1 polarities demonstrated that the crescent-shape often thought to indicate polarities in cells does not always correlate with polarities and can thus be sometimes misleading (Figure 1g). The method opens the way for a large scale study of accurate polarity dynamics at the scale of a whole tissue.

Acknowledgement

This work was supported by Human Frontier Science Program organization (HFSP) grant RPG0054-2013 and ANR grant 12-BSV6-0005 (AuxiFlo).

References

[1] E. Benkova, M. Michniewicz, M. Sauer, T. Teichmann, D. Seifertova, G. Jurgens, and J. Friml. Local, efflux-dependent auxin gradients as a common module for plant organ formation. *Cell*, 115(5):591–602, nov 2003.

[2] M. Botsch and L. Kobbelt. A Remeshing Approach to Multiresolution Modeling. In *Proceedings of the Symposium on Geometry Processing*, pages 185–192, 2004.

[3] R. Fernandez, P. Das, V. Mirabet, E. Moscardi, J. Traas, J.-L. Verdeil, G. Malandain, and C. Godin. Imaging plant growth in 4D : robust tissue reconstruction and lineaging at cell resolution. *Nature Methods*, 7:547–553, 2010.

[4] M. Garland and P.S. Heckbert. Surface simplification using quadric error metrics. In *SIGGRAPH '97*, 1997.

[5] W.E. Lorensen and H.E. Cline. Marching Cubes: A High Resolution 3D Surface Construction Algorithm. In *SIGGRAPH '87*, 1987.

[6] D. Reinhardt, E.-R. Pesce, P. Stieger, T. Mandel, K. Baltensperger, M. Bennett, J. Traas, J. Friml, and C. Kuhlemeier. Regulation of phyllotaxis by polar auxin transport. *Nature*, 426:255, nov 2003.

[7] J. Shi, J. Dong, J. Xue, H. Wang, Z. Yang, Y. Jiao, L. Xu, and H. Huang. Model for the role of auxin polar transport in patterning of the leaf adaxial-abaxial axis. *The Plant journal*, 92(3):469–480, nov 2017.

Statistical multi-scale atlasing of leaf morphogenesis

F. Selka[1], J. Burguet[1], E. Biot[1], T. Blein[2], P. Laufs[1], and P. Andrey[1]

[1]Institut Jean-Pierre Bourgin INRA, AgroParisTech, CNRS, Université Paris-Saclay, F-78000 Versailles, France
[2]Institut des Plantes Paris-Saclay, Gif-sur-Yvette, France

Abstract

How cellular mechanisms are integrated at the organ scale to orchestrate shape changes during morphogenesis remains largely unknown. Significant insights can be guaranteed by systematically quantifying the spatiotemporal evolution of 3D cell parameters in relation with the organ shape during the development. We developed a pipeline for multiscale statistical parametric maps of individual leaves, which provides an integrative view of factors involved at the cellular and the organ scale during leaf morphogenesis.

Keywords: Surface Parameterization, 3D Registration, 3D Atlasing, Leaf Morphogenesis.

1 Introduction

Because of the presence of a cellular wall, plant morphogenesis essentially results from the balance between differential cellular growth and division. This spatiotemporal regulation induce morphological and topological changes that contribute to the evolution of the organ shape. One challenge in developmental biology is to detect the emergence of cell populations with distinct characteristics that accompany the transformation of organ shape. Several studies have quantified 3D cell parameters in order to understand how cellular mechanisms contribute to organogenesis [1]. In particular, using leaf to study plant organogenesis, a framework was proposed to systematically quantify the cellular growth by mapping computed 3D cell parameters over the organ surface, thus providing a way to visualize and identify domains with distinct characteristics during development [5]. However, inter-individual variability at the cellular scale between organs at a given stage of development [7] can hide meaningful cellular growth patterns. To address this issue, a pipeline was proposed to integrate individual maps into statistical atlases showing the spatial distribution of average cellular parameters over average organ shapes [6]. A remarkable feature during aerial plant organs development is the reproducibility of their shape and size despite the heterogeneous growth that occurs at the cellular scale [3, 7]. Therefore, it is necessary to integrate organ shape and cell parameters of individual leaves at the same developmental stage to quantify their variability by providing 3D statistical maps. Based on the approach described in [6] for organ surface parameterization and registration, we show how we compute multiscale statistical parametric maps during development.

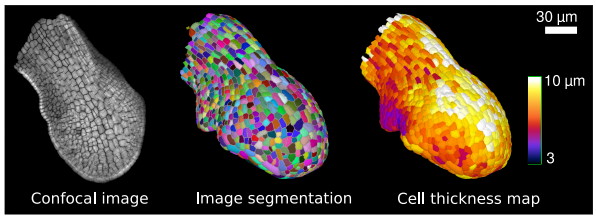

Figure 1: Data processing. (Left) 3D confocal image of a fixed leaf. (Middle) Results of watershed segmentation on epidermal cells; all sub-epidermal cells were unified into a single label. (Right) Results of mapping cell thickness.

2 Material and Methods

2.1 Image data and measurements

Developing leaves were fixed, stained and imaged using a confocal microscope, thus providing the outlines of cellular walls at the whole organ scale (Fig. 1, left). Images were segmented using a 3D watershed algorithm (Fig. 1, middle). Non-epidermal cells were merged into a unique "sub-epidermal" label. For each epidermal cell multiple morphological and topological parameters were measured including size, shape and the spatial organization of cells. As an illustration, Fig. 1, right shows the 3D map of epidermal cell thickness for an individual leaf. Parameter values were projected on the 3D leaf surface and displayed using a color look-up-table. In order to quantify the organ deformations during the development, we computed the mean surface curvature at each point within a neighbourhood of a radius of $30\mu m$.

2.2 Overview of the pipeline

Our parametric statistical maps are computed based on the following pipeline that proceeds in three steps: (1) computation

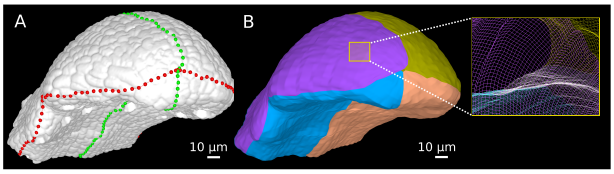

Figure 2: Overview of the surface parameterization method. (A) Leaf centered coordinate system computation defined by two axes: a lateral axis (Red) and a longitudinal axis (Green). (B) Parameterization of leaf surface using a quadrangular mesh.

of a leaf centered coordinate system based on the approach described in [6] (Fig. 2, A), separating the leaf surface into four quarters; (2) parameterization of each quarter (Fig. 2, B); (3) point-to-point registration and integration of parameters of individual leaves into prototypical leaf surface. In this paper, we describe how we compute the prototypical leaf surface and also shows how parameters of individual leaves are integrated and statistically mapped into prototypical leaf surface.

2.3 Prototypical shape computation and statistical parameters mapping

The surface parameterization is based on a standardized coordinate system and results in parameterized surfaces with the same number of points, which allow point-to-point registration [4]. Let $S_i^k = \{x_i^k(u,v), y_i^k(u,v), z_i^k(u,v)\}$ be the quadrangular surface of the k^{th} ($k \in \{1,\ldots,4\}$) quarter in the i^{th} leaf. The registration of N leaf surfaces is obtained by iteratively combining averaging and pairwise registration to the average shape in order to determine for each leaf i the rigid transformation T_i that minimizes the following error function [4]: $E(T_1,....T_N) = \sum_{i>j} \sum_{k=1}^{4} \parallel T_i(S_i^k) - T_j(S_j^k) \parallel^2$. The prototypical shape was obtained by averaging the four quarters across the registered leaves. Statistical parameters at corresponding vertices in the individual surfaces are computed for each corresponding vertex of the prototypical shape.

3 Results

Figure 3 illustrates the mapping of parameters at multiple scale for the cellular (average and variability of cell volume) and the organ level (surface curvature) over the prototypical leaf shape computed from five individual leaves at the same developmental stage with size between 350 and 400 μm. The integration of the individual measures into the average representation reveals a well delineated pattern of cellular parameter variations over the leaf surface. More particularly, the variability representation of cell volume reveals a pattern of cells at the distal part of leaf which also correspond to the regions where cells start to differentiate [2]. For each computed parameter, such a surface with projected values can be generated, thus providing a way to visualize and compare various cell and organ shape parameters during leaf development.

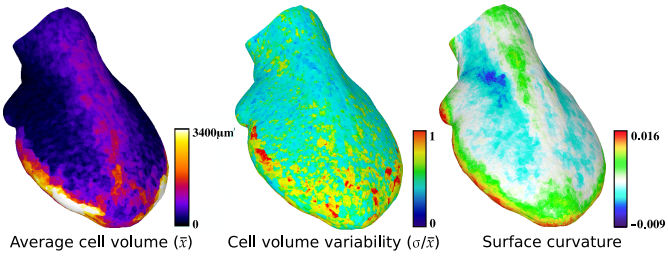

Figure 3: Surface rendering of prototypical leaf shape with a color rendering of average/variability cell volume and surface curvature values.

4 Conclusion

In this paper, we described a strategy to integrate multiple parameters at the organ and the cellular scale into 3D statistical maps. The obtained statistical representations are representative of the populations of shapes and provide atlases that will allow to correlate cell growth to the evolution of organ shape during its development. We believe these statistical atlases will be useful to extract robust principles and to elucidate the multiscale processes that subtend organ morphogenesis.

References

[1] G Bassel and R Smith. Quantifying morphogenesis in plants in 4D. *Curr Opin Plant Biol*, 29:87–94, 2016.

[2] Petra M Donnelly et al. Cell cycling and cell enlargement in developing leaves of arabidopsis. *Dev Biol*, 215:407–419, 1999.

[3] L Hong et al. Variable cell growth yields reproducible organ development through spatiotemporal averaging. *Dev Cell*, 38:15–32, 2016.

[4] E Maschino et al. Joint registration and averaging of multiple 3d anatomical surface models. *Comput Vis Image Underst*, 101:16–30, 2006.

[5] F Selka et al. Towards a spatio-temporal atlas of 3D cellular parameters during leaf morphogenesis. *ICCVW, 56-63*, 2017.

[6] F Selka et al. Surface parameterization and registration for statistical multiscale atlasing of organ development. *accepted in CVPRW*, 2019.

[7] L Serra et al. Heterogeneity and its multiscale integration in plant morphogenesis. *Curr Opin Plant Biol*, 46:18–24, 2018.

Statistical integration of image collection for modelling maize stem histology

David Legland[1], Fabienne Guillon[1], and Marie-Françoise Devaux[1]

[1]Biopolymères-Interactions-Assembages, INRA, Nantes, France

Abstract

Quantitative image analysis of plant tissues is fundamental to better understand the grinding performance or the microbial or enzymatic degradability of plant materials. The differences in size and shape between the stems complicates the integration of results. We propose a complete workflow for computing a statistical parametric mapping of cellular morphology. The workflow comprises the computation of a reference space, the projection of individual images into the reference slice, and the group-wise analysis of the registered images.

Keywords: Plant Histology, Parametric Mapping, Granulometry, Image fusion, Groupwise registration.

1 Context

Crop species like maize (*Zea mays L.*) are of increasing interest for cattle feeding or for production of bioethanol and biomolecules. Several mechanical, biochemical and/or enzymatic processes are involved to transform the raw material, mainly composed of the stem and the leaf cell walls, into energy or fuel.

The plant anatomy seems to play a key role in the plant biomass processes, and several investigations on stem histology have been performed [1,2]. However, the spatial distributions of quantitative features remain complicated to compare due to the differences in size and shape between the stems.

A strategy is to project all image data onto a common reference. Such an approach was developed for medical imaging [3,4], but few approaches exist for plant histology. In this study, we propose a complete workflow for statistical mapping of plant histology that comprises the computation of the reference slice from a collection of individual slices, the projection of each individual slice into the reference slice, and the group-wise analysis of the images after registration.

2 Material and methods

Ten maize internodes of the maxxis accession were sampled under the ear. Internodes were divided into twelve slabs of approximately equal thickness. Slab sections were extracted in either transversal or longitudinal directions, resulting in sixty stem cross-sections. Images were obtained using in-house macroscopy acquisition device, resulting in gray-level images with a resolution of 3.6 microns per pixel.

Parametric mapping of the cellular morphology was computed using localized granulometry analysis (Fig. 1). The contour of sections were segmented manually to take into account missing parts of sections. Centroidal Voronoi Diagrams with fixed number of germs were generated within the slice contours [5], resulting in convex regions of interest (Fig.1-b). Gray level granulometry curves obtained with mathematical morphology were computed for each region (Fig. 1c). An average cell size was associated to each region of interest, resulting in a parametric map of the typical cell size (Fig. 1d).

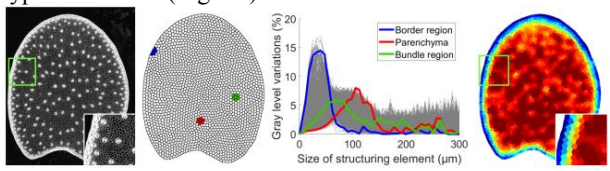

Figure 1. Parametric mapping of cellular morphology using gray-level granulometry. (a) Original image. (b) Partitioning of the slice into regular ROI. (c) Granulometric curve for each ROI. (d) Color-coded representation of the map of the typical cell size.

To compute the reference contour C_{ref}, the contour C_i of each slice was first manually delineated from images. Contours were centered, aligned to have vertical axis of symmetry, and rescaled to have the same area. The reference contour was then computed as the minimizer of the sum of the squared distances to other contours.

$$C_{ref} = \arg\min_{C} \sum_{i} d^2(C, C_i) \qquad (1)$$

The distance between two polygons is obtained by computing for each vertex of the reference contour the distance along the local normal to the individual polygon. The optimization procedure was performed by using an arbitrary contour as initial reference, and iteratively updating the coordinates of its vertices using eq. (1) until stability (Fig. 2a).

Once the reference contour is computed, each individual slice image must be transformed such that the contour C_i of the slice is superimposed with the reference contour C_{ref}. As the results requires interpolation within the individual image, we look for the reverse transformation that projects the reference contour on the individual contour.

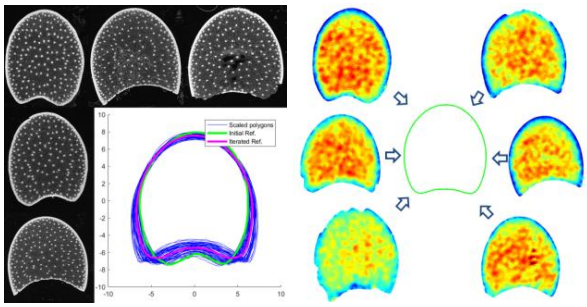

Figure 2. Computation steps for statistical parametric mapping of cellular morphology. (a) Computation of the reference contour from the collection of contours. (b) Projection of individual maps on the reference contour.

The transformation can be decomposed into an affine part that normalizes global changes, and a local model. Several local transformation models were investigated, including BSpline, polynomial, and radial scaling. Each family of transformations was parametrized by a parameter vector. The optimal transform was obtained by a applying the Nelder-Mead simplex optimizer over the parameter space. The optimization toolbox from Matlab was used.

Transformed images were obtained by iterating on pixels in the reference space, computing their projection within the individual image by using the reverse transformation, and interpolating within the individual image. Registration was applied both on the original images to validate the method, and on the parametric maps of cellular morphology (Fig. 2b).

3 Results

A parametric map of the cell size was obtained for each individual image (Fig. 1d). They were consistent with visual observation: large cells are located in the parenchyma, while small cells are located on the boundary and on the vascular bundles. A large heterogeneity could be observed, as well as variability between the slices (Fig. 2b).

An affine transform followed by a radial scaling model was chosen for registering images. The visual inspection of the reference contour registered on each individual contour showed that good superposition could be obtained, while maintaining smooth deformations at a local scale (Fig. 3a).

After registration, the parametric maps of cell morphology can be superimposed and group-wise analyzed. The statistical parametric map of cellular morphology obtained by computing the pixel-wise average shows the spatial distribution of the typical cell size within the reference section (Fig. 3b). Some results are similar to the ones observed on an individual image: small cells are located on the periphery of the slice, and large cells in the parenchyma. The vascular bundles are not visible anymore due to the global averaging. The cell size seems to be slightly larger in the middle of the parenchyma than in its periphery. It was also noticed that the layer of small cells on the sclerenchyma appears to be thinner on the lower part of the slice.

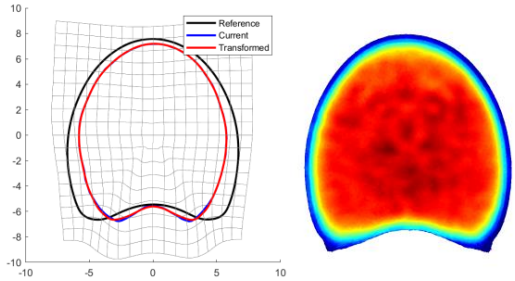

Figure 3. Results of image deformation. (a) Representation of the deformation computed for an individual image. (b) Statistical map of the cellular morphology obtained by integrating all the registered parametric maps.

4 Conclusions

We developed a framework for computing statistical parametric maps of cellular morphology from collections of images obtained on different stem sections. Results are consistent with visual observations, and make it possible to compare parametric mappings obtained with different experimental factors (growing conditions, genotypes, position within the internode…), while taking into account the biological variability. Future works aim at investigating the variations of parametric mappings of cell morphology with the position within the internode.

Statistical parametric mapping of plant histology opens new perspectives for a global analysis of collections of samples obtained on several individuals. Another perspective will be to compare statistical maps obtained from different imaging modalities, different stains, or different image analysis strategies [1,2]. Correlative imaging strategies can therefore be envisioned even if images are not acquired on the same samples.

References

[1] D. Legland, M.-F. Devaux, F. Guillon. Statistical mapping of maize bundle intensity at the stem scale using spatial normalisation of replicated images. PLoS ONE, 9(3), 2014.

[2] Y. Zhang, S. Legay, Y. Barrière, V. Méchin, V., D. Legland, Color quantification of stained maize stem section describes lignin spatial distribution within the whole stem. Journal of Agricultural and Food Chemistry, 61(13):3186–3192, 2013.

[3] U. Grenander and M. I. Miller. Computational Anatomy: an Emerging Discipline. Q. Appl. Math. 4:617-694, 1998.

[4] P. Thompson, R. Woods, M. Mega, A. Toga. (2000). Mathematical/computational challenges in creating deformable and probabilistic atlases of the human brain. Human brain mapping, 9(2):81-92, 2000.

[5] Q. Du, V. Faber, M. Gunzburger. (1999). Centroidal Voronoi Tessellations: Applications and Algorithms SIAM Review, 41:637-676

Accurate dating of organs during growth can unmask invariant developmental patterns: illustration with plant leaf morphogenesis

Mohamed Oughou, Eric Biot, Nicolas Arnaud, Aude Maugarny-Calès, Philippe Andrey, Patrick Laufs, and Jasmine Burguet

Institut Jean-Pierre Bourgin, INRA, AgroParisTech, CNRS, Université Paris-Saclay,
78000 Versailles, France

Abstract

Living organisms produce organs with shapes both stereotyped and affected by variability. Further, final organ shape is the result of biological mechanisms integrated in space and time. Morphogenesis analysis thus requires reliable dating system. We propose to use organ size to trace back to its age. This allows the conjoint analysis of organs sampled in different organisms, and the comparison of leaf development, e.g., from different genotypes. We analyzed leaf shaping in the plant *Arabidopsis thaliana*. Our results suggest that morphogenesis of leaf blade and serrations are, at least partially, decoupled.

Keywords: Leaf Shape, Leaf Margin, Plant Growth, Multi-scale Analysis.

1 Introduction

The proper analysis of organ morphogenesis requires accurate dating of the organ itself and of significant events during development, e.g., the emergence of a tooth at the boundary. Here we propose a strategy to date any organ based on its size. For this, we determine the initiation date of any organ during the organism lifetime, and we model the growth dynamics using a function relating organ size and age. Thus, it is possible to compute the age of an organ by considering its size. Then, individual organs can be registered in time and different organs compared, e.g., coming from different genotypes. We also propose to detect and date the development of important features during growth, like the appearance of particular shape patterns. We illustrated this strategy in two dimensions to analyze the leaf development. Our results showed that different teeth, i.e. successive ones in a given leaf or the same one in different leaves, follow very similar development processes, and we also revealed subtle differences between them.

2 Dating leaf growth dynamics

Here, we used leaves that appear successively in the rosette of the plant *Arabidopsis thaliana*. We consider that leaves are ordered according to their apparition, so that a leaf of rank i (leaf i) refers to the i-th leaf that emerged. We also used this classification to order the teeth appearing successively: the tooth of rank i is the ith to emerge.

We first propose a means to compute, for any individual leaf, the age of the organ from its initiation. For this, we compute the function that links its age to its size, typically the blade length. First, plastochron measures are performed to determine the initiation date of organs (Fig. 1A). Next, based on the pairs of measures plant age-leaf length, we model the function relating plant age to leaf blade length with a Hill function (Fig. 1B). Then, we obtain the relation between leaf age and length.

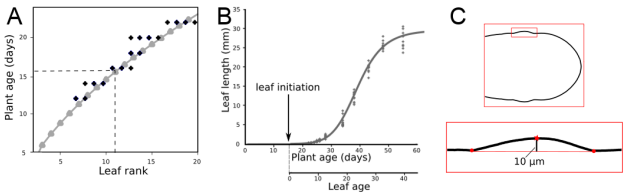

Figure 1: Dating the leaf. (A) Leaf primordia are counted at different dates and a polynomial function is fitted. (nitiation of leaf 11 $\approx$ 15.6 days. (B) The relation between leaf length and plant/leaf ages is modeled with a Hill function. (C) The criterion to detect tooth initiation is a minimum height of 10μm.

To analyze leaf serrations, we also propose to date the emergence of individual teeth. For this, we set a height threshold that determines the tooth initiation time (Fig. 1C).

3 *Arabidopsis thaliana* leaf shaping

Leaves in the rosette have different overall sizes and shapes, and present different degrees of serration at the margin. First

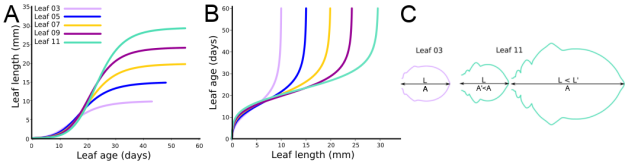

Figure 2: Growth dynamics of leaves in the rosette of *Arabidopsis thaliana*. A: leaf length as a function of leaf age for leaves of odd ranks between 3 and 11. B: leaf age as a function of leaf length. C: comparison of leaves of ranks 3 and 11 with either the same length L or the same age A.

leaves have rather round shapes with few serrations, while it becomes more and more elongated with more teeth as the rank increases. We focused here on leaves of odd ranks going from 3 to 11 presented in a previous work [1].

Results are displayed in Figure 2. Differences in growth kinetics between the ranks clearly appeared (Figs. 2A and 2B). Final blade length are significantly different (the higher the rank, the longer the blade), while, during early phases, the order is reversed (higher ranks leaves are smaller than lower rank ones). These differences could be explained by a trade-off between cell proliferation early in the development and cell differentiation that occurs later on. High rank leaves could thus stay longer at a proliferation state and then initially grow slowly, while because they generated more cells, their final shapes are bigger than low rank leaves. The necessity to take real leaf age instead of organ size as a proxy of time was illustrated in Fig. 2C, which shows that two leaves of the same size may have significantly different ages. Our results illustrated the necessity to consider the whole development to fully characterize the organ shaping.

Next, we compared serration development at the margin (Fig. 3). When expressed according to leaf length (Figs. 3B and 3E), morphological measures of successive teeth in the same leaf suggested that they follow distinct growth trajectory. Yet, with appropriate time measure (Figs. 3CD and 3FG), it appeared that teeth grow with similar dynamics, both in width and height. These results emphasized subtle differences, e.g., the fact that growth in height stops earlier in lower rank teeth.

Second tooth morphology was evaluated in leaves with different ranks. As for tooth width (Figs. 3H), we showed that they grow at the same rate in all leaves. Conversely, they grow differently in height (Figs. 3I), and the tooth is more pointed in higher rank leaves (Figs. 3J).

4 Conclusions

In conclusion, we illustrated here that the proper dating of the development allows to finely analyze the shaping of organs, both at global (whole organ) or local (serrations) scales. In particular, we can reveal subtle events that occur during the organ growth.

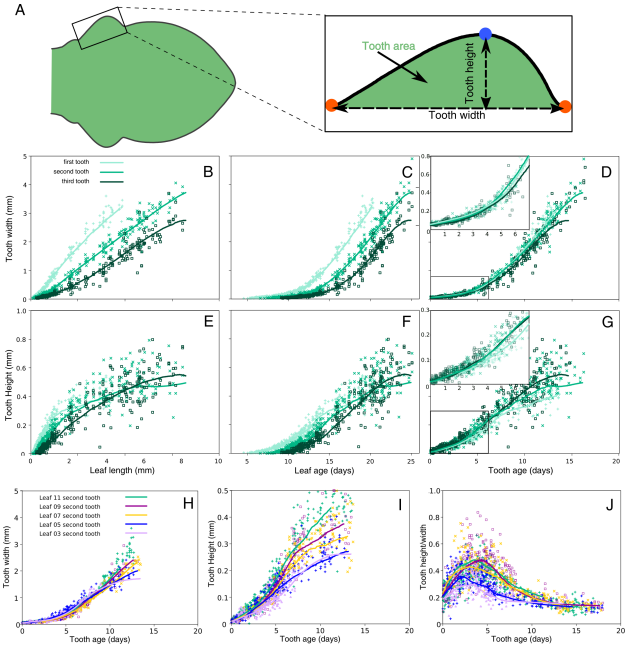

Figure 3: Morphological serration parameters. B-G: tooth width (B-D) and height (E-G) in individual leaves (dots) and in leaf growth trajectories (curves), plotted either against leaf length (left), age (center) and tooth age (right). H-J: second tooth measures for different leaf ranks according to tooth age. H: tooth width; I: tooth height; J: height/width.

Appropriate dating also allows the integration of individual organs sampled in different organisms, and the comparison of the developments of different organs. Lastly, it should be pointed out that growth dynamics functions have to be recomputed each time for different leaves (ranks/genotypes/growth conditions...). However, this procedure is rather straightforward, and this is commonly done in our lab.

Acknowledgment

The Jean-Pierre Bourgin Institute benefits from the support of the Labex Saclay Plant Sciences-SPS (ANR-10-LABX-0040-SPS). MO was funded by the Île-de-France regional PhD grant. We thank the IJPB OV-Cytologie/Imagerie platform the for the microscopy facilities.

References

[1] Biot et al., Multiscale quantification of morphodynamics: Morpholeaf software for 2d shape analysis. *Development*, 143(18):3417–3428, 2016.

Image based phenotyping for wheat vitality

Andreas Honecker[1], Henrik Schumann[1,*], Diana Becirevic[2], Lasse Klingbeil[2],
Kai Volland[3], Steffi Forberig[3], Hinrich Paulsen[3], Heiner Kuhlmann[2] and Jens Léon[1]

[1]INRES - Plant Breeding, University of Bonn, Katzenburgweg 5, 53115 Bonn, Germany
(honecker, h.schumann, j.leon)@uni-bonn.de
[2]IGG - Geodesy, University of Bonn, Nussallee 17, 53115 Bonn, Germany
(becirevic, klingbeil, kuhlmann)@igg.uni-bonn.de
[3]terrestris GmbH & Co. KG, Kölnstraße 99, 53111 Bonn, Germany
(volland, forberig, paulsen)@terrestris.de

Abstract

Image assisted phenotyping plays a major role in future plant breeding. We introduce a new method for characterization of wheat vitality, based on images of 12 winter wheat varieties and captured with standard RGB cameras under field conditions. An automated image processing pipeline using machine learning approaches quantifies dead, chlorotic and vital pixel area of the plants. Measuring large areas within plots we improve phenotyping precision and representativity and accelerate phenotyping throughput. The ability to import, store and visualize plant vitality data and corresponding images within our new information system CropWatch enables breeders to directly benefit from image based phenotyping.

Keywords: Phenotyping, Wheat Vitality, Image Processing, Machine Learning, Information System

1 Introduction

Image assisted phenotyping is considered a key technology in plant science [1], opening opportunities for improved selection of breeding material and development of superior elite varieties [2], finally leading to improved agricultural productivity [3]. During the vegetation, several biotic and abiotic factors, such as drought, heat and malnutrition affect wheat vitality. These factors result in a proportion of vital to stressed regions, from green to yellow to brown parts of the plant, especially its leaves (Fig.1).
Here, we introduce a method to measure this plant vitality based on RGB-images.

2 Material and Methods

Expecting differences in their vitality, we selected 12 European elite wheat varieties registered between 1968 and 2014.
Images were captured from 2m distance to canopy with a standard RGB camera (Canon EosD1200). Each image captured covers approximately 1m² per plot, with an edge length of about 0.25mm per pixel, additionally including a color reference chart (X-Rite ColorChecker Classic).
The camera was mounted to our tractor based field phenotyping platform, which is covered with translucent fabric, minimizing and homogenizing shading, but still allowing light to pass into the scene, in order to forgo artificial light sources. To analyze images, an image processing pipeline (IpP) was developed in Python 3.6. The IpP directly accesses a folder structure where images and their geographic(geo) coordinates are stored.
After automated import of images, IpP runs over following steps: Rescaling to exclude distorted image areas - Generation of feature matrix - Classification of plant and non-plant pixels - Masking of non-plant pixels - Selection of hue channel from HSV color space - Generation of color clusters - Resulting trait: Plant pixel area (%) per color cluster - Export of results as csv-file.
After processing in IpP, resulting data, images and the corresponding geo-coordinates are imported to our newly developed data management and information system CropWatch.

Figure 1 Magnified section from an unprocessed image

* Corresponding author

Table 1 Classification result for plant and non-plant pixels

	Plant	Non-Plant	Accuracy (%)
Plant	13480162	32002	99.7 %
Non-Plant	93605	7206731	98.8 %

3 Results and Discussion

With our phenotyping platform we are able to capture our trial with 96 plots and 3 images per plot in 1 hour. During vegetation period we repeated this on 2 locations every 2 weeks.

Due to the fabric the images showed sufficient contrast and homogeneous shading (Fig.1), thus minimizing environmental effects.

The computationally most intensive and obviously crucial step of processing was the reliable identification of plant pixels. Classification of plant and ground was achieved using a support vector machine. Images were transformed to a 27-dimensional feature matrix, including pixelwise neighborhood statistics and color features, with resulting 9 dimensions of significant impact on the classifier. We performed tests comparing classifiers, finally selecting a random forest classifier with 100 decision trees providing the best classification result. According to the confusion matrix, we achieved an overall classification accuracy of more than 99% (Tab. 1).

According to an earlier approach with single wheat leaves captured without environmental influences by a document scanner, we clustered the plant pixels using HSV color spaces hue channel. While 0°-4° was not used, to exclude artificial or sensor errors in the images, 5°-60° was defined as "Dead" (red-brown-yellow), 61°-75° as "Chlorotic" (yellow,greenish-yellow) and 76°-200° as "Vital" (yellowish-green, green and blueish-green).

For the 12 wheat varieties, we measured significant variation in plant pixel area with 5-9% for "Dead", 17-25% for "Chlorotic" and 65-78% for "Vital" pixel area (Fig.2). This demonstrates that selection of vital or stress tolerant wheat varieties will be possible with our method.

As we capture 3 images per plot, resulting in nearly 3 m² covered area (up to 25-50% of a normal breeding plot), precision, representativity and therefore reliability of such measurements highly increases in relation to point measurements with handheld devices or traditional scoring.

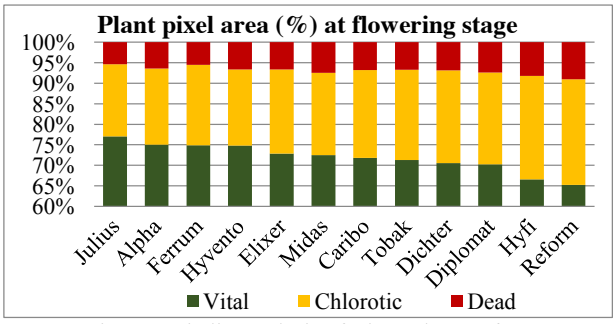

Figure 2 Vitality analysis of wheat plant surface

Due to the integrated color reference, we were able to homogenize images within and over different dates, allowing us to do comparable time series of color development during the whole vegetation period.

With the web-based data management system CropWatch, we are able to import, store and visualize all kinds of raw and processed images, as well as the extracted plant color parameters. These can be shown either as customized data tables and figures, or visualized on maps due to geo referencing of data. Additionally, it is possible to check conspicuous data in the corresponding original image.

4 Conclusion

Climate change effects cause intensive efforts in plant breeding to select more vital and stress tolerant genotypes for adaptation to stronger variation in weather. With this RGB-image based method we can offer objective, precise and reliable measurements of plant surface vitality of wheat and replace subjective scorings. This is not only possible at one certain growth stage, but during the whole vegetation process, to characterize a variety regarding stress response or stay-green potential during maturation.

With the current setup more than a hundred large plots can be covered in one hour, having the processed data available the next day. Compared to traditional phenotyping, throughput is accelerated and time and manual workload can be saved during the labor-intensive field season in plant breeding.

The possibility to store the images and resulting color parameters in the data management system CropWatch, together with relevant agronomic data from soil, weather, fertilization and yield generates valuable information for breeders selection decisions [3]. Due to geo referencing of data, identification and addressing of stress hot-spots is possible and can enable site-specific fertilization and plant protection and improve precision farming techniques.

Acknowledgements

German federal ministry of agriculture for funding (FKZ 2.815.702.315.00) and teams from University Campus Klein-Altendorf and Poppelsdorf for their help in field trials.

References

[1] F. Fiorani and U. Schurr. Future Scenarios for Plant Phenotyping. Annu. Rev. Plant Biol. 64:267–91, 2013

[2] J.L. Araus, S.C. Kefauver and J.E. Cairns. Translating High-Throughput Phenotyping into Genetic Gain. Trends in Plant Sci. 23:451-466, 2018.

[3] J.L. Araus and J.E. Cairns. Field high-throughput phenotyping: the new crop breeding frontier. Trends in Plant Sci. 19:52-61, 2014.

Measurement Method of Leaf Morphology Based on Point Cloud Data

Chunying Wang[1,2], Baohua Liu[1,2], Xiang Li[3], and Ping Liu[1,2*]

[1]School of Mechanical and Electronic Engineering, Shandong Agricultural University, Taian, China
[2]Shandong Provincial Key Laboratory of Horticultural Machineries and Equipments, Taian, China
[3]State Key Laboratory of Crop Biology, College of Life Sciences, Shandong Agricultural University, Taian, China
wcychunying@126.com(Chunying Wang); 18706388907@163.com(Baohua Liu); lixiang@sdau.edu.cn(Xiang Li);
liupingsdau@126.com(Corresponding author: Ping Liu)

Abstract

In order to monitor plant growth and obtain the morphology of curved leaf, a new measurement method of leaf morphology was proposed based on point cloud data. By using Agglomerative Nesting and cubic interpolation method to segment point cloud and reconstruct leaves, individual leaves morphology was estimated. Compared with manual measurement, leaf azimuthal angle, length, and area estimations were in a good agreement ($R^2 > 0.996$). But estimation of leaf inclination angle was low-correlated due to the error of manual measurement. Results show that the proposed method could accurately estimate the morphology of curved leaves.

Keywords: Plant Leaf Morphology, Growth Monitoring, Hierarchical Clustering, Point Cloud Data

1 Introduction

Plant structure is an indicator of the growth and development status of a plant as it continuously adjusts to a dynamically changing environment [1]. Leaf morphology objectively reflects its physiological conditions, including leaf angle (leaf inclination and azimuthal angles), length, and area, which is critical in determining the plant structure, and subsequently the photosynthetic productivity [2]. To improve yield and the adaptation abilities of plants to climate change, the plant growth state is assessed by measuring leaf morphology.

Several technologies have been developed for non-contact measurement of plant morphology, including machine vision [3], stereo imaging, laser scanning [4] and depth image [5]. Researchers have used the non-invasive methods to collect point cloud data of plant structure, which could restore the plant space surface information. But the current study could not solve the problem of inaccurate measurement of curved leaf morphology.

In this paper, ordinary plants with curved leaves (Spathiplyllum) were taken as the research object. The proposed measurement method of curved leaf morphology is shown in Figure 1. The point cloud data were preprocessed according to the height to remove the ground data noise. Hierarchical clustering [6] and cubic interpolation methods were used to segment the point cloud and reconstruct leaves. Leaf morphology was estimated based on the structure characteristics of leaf individual leaves, which provided a research basis for plant growth monitoring based on machine vision. We also manually measured leaf morphology to assess the proposed measurement method accuracy of curved leaf morphology.

2 Material and Methods

The laser HIREED703A was used in this paper to collect point cloud data of plants. Firstly, the point cloud data were preprocessed according to the height to remove the ground data noise. Then, the hierarchical clustering method named Agglomerative Nesting (AGNES) [7] was adopted for leaf segmentation. The AGNES constructs a hierarchy of clusterings. Each observation is a small cluster by itself. At each stage, the two nearest clusters are combined to form one larger cluster. AGNES requires to specify input parameters: the number of clusters k and clustering distance measure function d given in equation (1).

$$\begin{aligned} d_{min}(C_i, C_j) &= \min_{X \in C_i, Z \in C_j} dist(X, Z), \\ d_{max}(C_i, C_j) &= \max_{X \in C_i, Z \in C_j} dist(X, Z), \\ d_{avg}(C_i, C_j) &= \frac{1}{|C_i||C_j|} \sum_{X \in C_i Z \in C_j} dist(X, Z), \end{aligned} \tag{1}$$

where C_i is a cluster, X=Z is the point data. Lastly, the cubic interpolation method was used to fit the segmented point cloud of leaves. The leaf was approximated as a space surface.

The average inclination angle was calculated by weighting the segmented leaf area A_i using equation (2). α_i is the angle between the main leaf vein and the horizontal plane. Leaf azimuthal angles β is the angle between the main leaf vein and the north direction.

$$\alpha = \sum_{i=1}^{n} \omega_i \alpha_i \tag{2}$$

$$Area = A/cos\alpha \tag{3}$$

$$L = l/cos\alpha \tag{4}$$

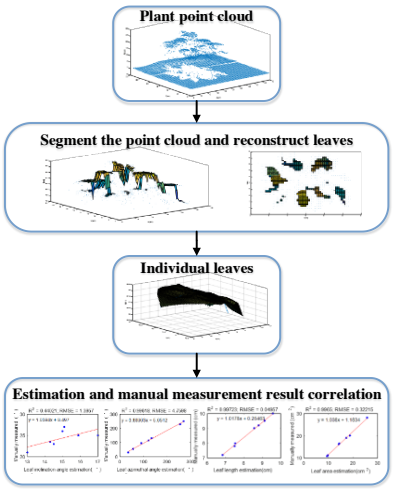

Figure 1: Measurement Method of leaf Morphology Based on Point Cloud Data

The weight $\omega_i = \frac{A_i}{A}$. A is the area of leaf projected onto a horizontal plane. Number of segments of leaf is set according to the leaf shape. The real area and length of leaf could be obtain using equation (3, 4), where l is the length of the main leaf vein projected onto a horizontal plane.

3 Results and Discussion

Plant leaf morphology (leaf angle, length, and area) were retrieved based on point cloud data of individual leaves. Figure 2 shows the values scatter plots between the leaf morphology of individual leaves estimations and manually measured.

The leaf azimuthal angle, length and area estimations were in a good agreement with values obtained from manual measurements (R^2 = 0.996, RMSE=4.7587°; R^2 = 0.997, RMSE = 0.04957cm, and R^2 = 0.997, RMSE = 0.32215cm^2, respectively). The estimation of leaf inclination angle was low-correlated (R^2 = 0.44021, RMSE=1.3957°). Note that angle measured by manual measurement of the curved leaf cannot truly reflect leaf shape, so the estimations of leaf inclination and azimuthal angle were considered accurate.

4 Conclusions

In this paper, the measurement method of leaf morphology based on point cloud data was constructed. By using AGNES and cubic interpolation method, leaves were segmented and reconstructed. The comparison results demonstrated that the proposed measurements could estimate curved leaves morphological with higher precision (leaf morphology R^2 were 1.3957°, 4.7587°, 0.04957cm, and 0.32215cm2, respectively). In the future, we will continue to improve the blade segmentation method. Plant morphology measurement method based on reconstruction of plant point cloud will be developed to provide technical support for plant growth monitoring.

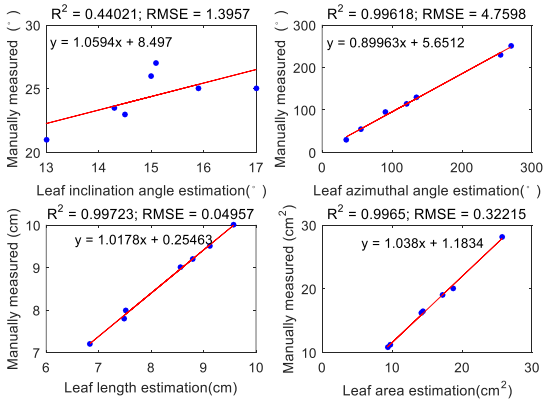

Figure 2: Scatter plots between the leaf morphology of individual leaves estimations and manually measured.

Acknowledgement

The work was supported by the National Natural Science Foundation of China (No. 31700644), the Funds for Young Teachers' Growth Program of Shandong Agricultural University, and Postdoctoral Science Foundation of China (Nos. 2015M582122240; 2016T90644).

References

[1] W. Fang, H. Feng, W. Yang, L.F. Duan, G.X. Chen, L.Z. Xiong, Q. Liu. High-throughput volumetric reconstruction for 3D wheat plant architecture studies. Journal of Innovation in Optical Health Science, 2016, 09(05): 13.

[2] A.J. Burgess, R. Renata, H. Tiara, E.H. Murchie. Exploring Relationships between Canopy Architecture, Light Distribution, and Photosynthesis in Contrasting Rice Genotypes Using 3D Canopy Reconstruction. Frontiers in Plant Science, 2017, 8: 734-749.

[3] B.S. Kumar, V. Vijayan, J.P. Davim. Machine Vision in Measurement. 2019.

[4] Y.M. Li, Y.J. Su, T.Y. Hu, G.G. Xu, Q.H. Guo. Retrieving 2-D Leaf Angle Distributions for Deciduous Trees From Terrestrial Laser Scanner Data. IEEE Transactions on Geoscience and Remote Sensing, 2018: 1-11.

[5] Y. Jiang, C.Y. Li, A.H. Paterson. High-throughput Phenotyping of Cotton Plant Height using Depth Images under Field Conditions. Computers and Electronics in Agriculture, 2016, 130: 57-68.

[6] W. Wei, J.Y. Liang, X.Y. Guo, P. Song, Y.J. Sun. Hierarchical division clustering framework for categorical data. Neurocomputing, 2019, 341(14): 118-134.

[7] L. Kaufman, P.J. Rousseeuw. Agglomerative Nesting (Program AGNES). 1990.

Revisiting SIFT for plant foliage in RGB images acquired on a turntable

Helin DUTAGACI[1], Etienne BELIN[1,2], and David ROUSSEAU[1]

[1]LARIS, UMR INRA IRHS, Université d'Angers, 62 avenue Notre Dame-du-Lac, 49000, Angers, France.
[2]Plate-forme PHENOTIC, SFR 4207 QUASAV, IRHS, UMR1345, Université d'Angers, F-49045, Angers, France.

Abstract

In this work, SIFT features are revisited for their use in two applications of computer vision for plant analysis. The first application is the reconstruction of 3D models of plants through tracking homologue points in successive intensity images. The second application is to provide a new global descriptor that gives a measure of the level of self-similariy of foliage for plants of different architectures and foliar appearance. In order to properly exploit SIFT descriptors in relation to these applications, we discuss two aspects of the classical SIFT keypoint matching practice. On the one hand we propose to match detected keypoints based on a scale criterion. On the other hand, we drop the ratio rule while matching keypoints in two images and propose the use of a spatial proximity filter instead.

Keywords: Image Processing, SIFT, Self-Similarity, Plant Foliage.

1 Context

Scale Invariant Features Transform (SIFT) has been introduced with a biologically inspired philosophy [1] to reproduce the human capability to recognize objects when observed at various scales. SIFT achieves this scale invariance with local features mimicking the way the human eye captures information locally via the fovea [2]. This local feature encoding has been demonstrated to be very useful, for registration of cluttered images and for object recognition. However, an issue rarely discussed while using SIFT in such context is that biological structures are very self-similar and multi-scale. This is specially the case for plants which grow, by design, with replication of branches and leaves which may all be very similar [3]. In this context, we revisit SIFT to raise interest on the issues of scale-dependency of SIFT and the matching scheme of the keypoints, both to characterize the self-similarity of foliage and to provide correct homologue point matches between successive images for 3D reconstruction. We illustrate our approach with plants positioned on a turntable and imaged with a color camera.

2 Using SIFT keypoints to match homologue points

Detection of homologue matches between images of plants is an important step for capturing the 3D geometry through, for example, structure from motion, or from turntable image sequences. The number of correct matches between views has a high impact on the estimation of camera poses. The self-similarity of plants contributes in a negative way to the correct matching of homologue points between views. A demonstration is shown in Figure 1. The keypoints in two consecutive frames from the turntable sequence are matched using the classical SIFT keypoint matching scheme described in [1]. Considering that SIFT yields few stable keypoints in low-resolution images, incorrect matches due to self-similarity in plants have a detrimental effect on estimating camera parameters. Furthermore, Lowe's ratio rule [1] has a negative effect for plant images possessing repetitive structures. The ratio rule states that a match between two images is valid only if the ratio between the descriptor distance between the first and second candidates is lower than a threshold. This condition fails often for plants due to self-similarity. For image sequences of plants where the camera movement is small, we drop the ratio rule and use an alternative matching scheme for successive images. For each keypoint in the first image, only spatially close keypoints in the second image are considered for matching. We further filter the candidate keypoints by scale and only allow matches within 0.5 scale difference. The filtered candidates with a descriptor difference below a threshold are accepted as matches.

3 Using SIFT keypoints to evaluate self-similarity

The SIFT keypoints can also be used to measure the self-similarity of the foliage with an alternative matching strategy. Self-similarity in this context can be described as the amount of repetitive patterns within and between views. A four-steps method is proposed to quantify the amount of similar, but not

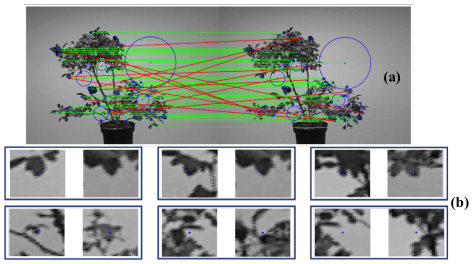

Figure 1: (a) Matched SIFT keypoints in two consecutive frames from a turntable sequence. The ratio rule in [1] was used. Red lines indicate non-homologue matches. The size of the blue circles indicates scale. (b) Example pairs of non-homologue matches from (a).

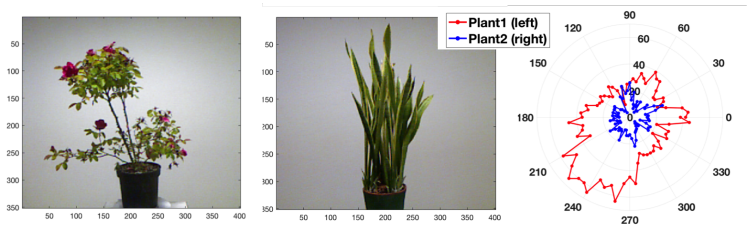

Figure 2: On the left: 2 plants ('Queen Elisabeth' rosebush and 'Sanseviere' houseplant) with different foliage appearances. On the right: polar plot of the self-similarity (amount of similar keypoints) of the 2 plants according to the angle position of plants on the turntable.

spatially homologue, keypoints. The first step is the tuning of parameters (octave, first layer, number of layers) of the SIFT computation for one image. It provides an image represented by a collection of keypoints (and descriptors) at an adapted scale, where one reference keypoint associated to a leaf can be defined. The second step consists of comparing the descriptors of the other keypoints to the reference by Euclidean distance then filtering keypoints by thresholding distances according to the mean distance between all descriptors in this image. In the third step, we count all the filtered keypoints, which are considered to be similar to the reference keypoint. In the fourth step, we repeat the second and third steps on all the images from the turntable i.e. 72 images (1 image / 5 degrees = 360 degrees) to count the amount of similar keypoints and we plot these values in polar representation as illustrated in Figure 2.

To test the relevance of this approach, we choose to apply this method on two plants with different foliar appearance. We can observe that plant 1 ('Queen Elisabeth' rosebush) has a complex architecture with many branches leading to a large number of leaves and a wide distribution of them throughout the plant. The plant also has a non-symmetrical geometry. Plant 2 ('Sanseviere' houseplant) has a simpler architecture, vertically tubular, with tight leaves distributed relatively uniformly around the central axis of the plant. The polar curves in Figure 2 exhibit different amplitudes: plant1 (red curve) has higher amplitude than plant 2 (blue curve). Such amplitudes can then be interpreted as other quantitative descriptors complementary to the ones (effective volume, spatial symmetry and lacunarity) introduced in [4] to characterize the global appearance of the plant foliage.

4 Conclusion

We modified the classical matching scheme of the SIFT method by removing the ratio rule and introducing scale and spatial constraints to reduce the effect of self-similarity on the number of homologue matches between successive images of plants. We also employed scale-dependent matching of keypoints at certain scales to estimate the self-similarity of foliage as the amount of repetitive patterns throughout the plant views.

References

[1] R.G. Lowe, "Distinctive image features from scale-invariant keypoints," *International Journal of Computer Vision*, vol. 60, 91–110, 2004.

[2] A. Delahaies, D. Rousseau, J.B. Fasquel, F. Chapeau-Blondeau, "Local-feature-based similarity measure for stochastic resonance in visual perception of spatially structured images," *Journal of the Optical Society of America A*, vol. 29, 1211–1216, 2012.

[3] D. Rousseau, Y. Chéné, E. Belin, G. Semaan, G. Trigui, K. Boudehri, F. Chapeau-Blondeau, "Multiscale imaging of plants: current approaches and challenges," *Plant Methods*, vol. 11, 6, 2015.

[4] Y. Chéné, D. Rousseau, E. Belin, M. Garbez, G. Galopin, F. Chapeau-Blondeau, "Shape descriptors to characterize the shoot of entire plant from multiple side views of a motorized depth sensor," *Machine Vision and Applications*, vol. 27, 447–461, 2016.

Shape modeling of wheat grain through its development

Thang Duong Quoc Le[1], Christine Girousse[2], David Legland[1], and Anne-Laure Chateigner-Boutin[1]

[1]UR1268 BIA, INRA, Nantes, France
[2]UMR GDEC, INRA, Université Clermont-Auvergne, Clermont-Ferrand, France

Abstract

Quantifying the changes in morphology of wheat grain across development is essential to better understand the factors limiting its growth. In this work, we investigated such changes using X-ray micro computed tomography (μCT) and 3D digital image processing. We developed a robust semi-automatic image processing methods for identification of 3D wheat grain and extraction of grain morphometry. We also proposed an approach to construct an average grain as a representative shape for each developmental stage. The quantitative description of morphology and of the average grain enlights the differences of growth within the grain. These first results will help build a developmental atlas of wheat grain based on 3D imaging data.

Keywords: X-ray μCT, 3D image analysis, 3D shape modeling, wheat, *Triticum aestivum* (L.).

1 Introduction

Wheat is one of the most important crops worldwide. Grain size and shape are two important grain traits that impact grain yield and milling performance. Both traits are established during grain development. Therefore, the quantitative description of changes of grain morphology through its development should help to identify factors limiting the growth.

3D images of wheat grains can be acquired from X-ray micro-computed tomography (μCT) [1]. 3D image analysis can be applied to obtain quantitative data describing the grains [1]. However, most works focused on mature dry grains, and the quantitative morphology of developing wheat grains remains largely unknown.

We investigated X-ray tomography to quantify changes of morphology of wheat grain during its development. The approach comprises a semi-automated workflow for 3D segmentation and quantification, and the construction of a statistical shape model that depicts the global changes of shape.

2 Methods

Images of wheat grains at various stages were obtained using X-ray μCT tomography. We developed an image segmentation workflow to identify the wheat grain within 3D μCT image. The segmentation process included automated selection of threshold from a multimodal histogram, selection of regions based on size criterium and morphological filtering. We extracted several morphometric features of individual wheat grains: grain's dimensions, volume of the different tissue regions. In addition, we developed a specific workflow for quantifying the shape of the grain crease based on the variations of crease depth along grain length [2].

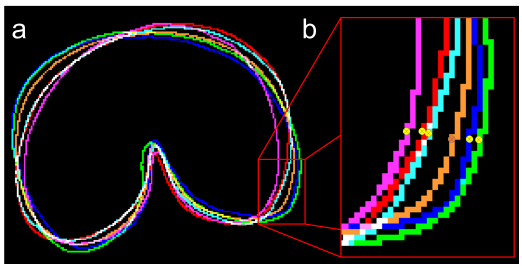

Figure 1: Construction of the average grain for a developmental stage. **a** Result of the shape alignment using ICP algorithm [3]; **b** Each point in the average shape (the orange curve) is the average of correspondences between grain shapes and the reference shape (the blue curve).

In order to take into accound the biological variability between grains of a same developmental stage, we developed an approach for the construction of an average grain shape model for each stage of development. The 3D binary images of wheat grains were converted to 3D point clouds. The point clouds in the same stage of development were aligned to a reference shape using principal axis alignements followed by an Iterative Closest Point (ICP) algorithm [3] (Fig. 1a). The reference shape was chosen as the grain whose length is the closest from the population average. The ICP algorithm finds the best rigid transformation (i.e. using only translation and rotation) that projects an indiviual point cloud onto the reference point cloud, by minimising the distances between corresponding points. The initial average shape was computed by taking the average of cor-

respondences between the initial reference shape and respective shapes of the population (Fig. 1b). Finally, the average grain corresponding to the Fréchet mean [4] was computed using the following procedure: The initial average shape was chosen as the reference. The grain shapes were re-aligned using the ICP algorithm to the reference shape. The new average shape based on the re-aligned shapes was computed. The procedure was iterated until the average distance of individual shape's vertices to average shape reaches stability.

Shape variability maps were also considered to investigate the biological variability. For each vertex of the average grain, the distances d_i to each individual point cloud were measured. The average of the distances d_i was used as a variability measure of each vertex.

3 Results

The X-ray μCT allowed the 3D image acquisition of whole grains for all considered stages of development and the observation of the grain internal structures. The 3D images highlighted the evolution of the grain shape during development: the grains of early stages present an inverted triangle shape with a large roll (Fig. 2a), then the grain elongates to form an ellipsoid (Fig. 2c). At later stages, the lobes thicken.

The initial average grain was constructed for each stage of development (Fig. 2b, d). The resulting shape was similar to a typical grain of the corresponding stage. The global shape is more smooth, but it retains many fine structures, especially around the rolls. The shape of the crease is also well preserved. The variability measure of each vertex of the average grain ranged from 0.01 – 0.13 mm at stage 60 °DAA and 0.02 – 0.17 mm at stage 310 °DAA (Fig. 2). The average shape variability is approximately 0.04 mm at stage 60 °DAA and 0.07 mm at stage 310 °DAA respectively. It depicts the representative shape of a grain population in a developmental stage. It enabled us to identify the regions of the grain that exhibit the distribution of local shape variation around the average shape.

4 Conclusion and Perspectives

In this study, we shows that X-ray μCT acquisitions and image processing methodologies has great potential for investigation on morphometry of developing cereal grain. The morphometry analysis of wheat grains will be completed by additional features such as surface area, symmetry factor, or local curvatures. The average of wheat grain describes variability in the shape and size in each developmental stage of the wheat grain population. Further work will focus on the computation of average grains using non rigid transform models, and on the construction of a 4D (3D + time) developmental atlas of wheat grain throughout its development based on average grains generated for each developmental stage.

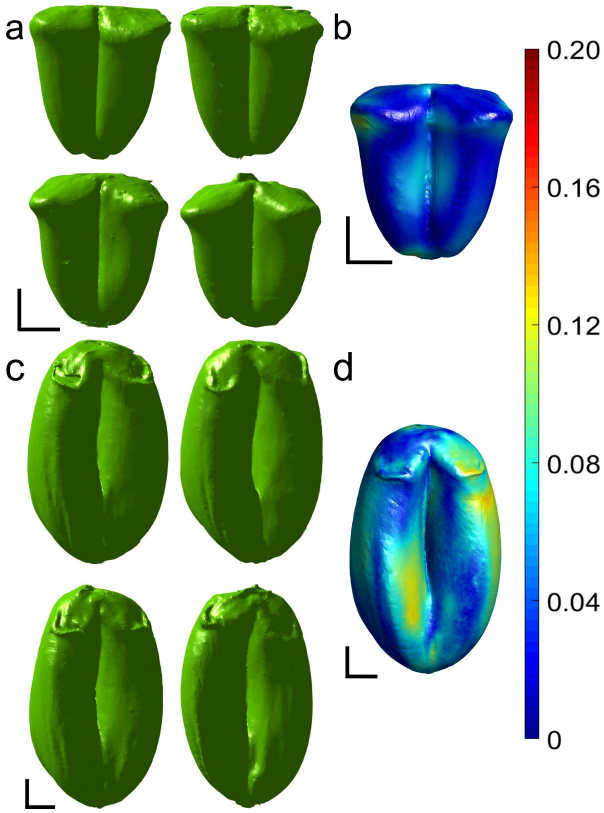

Figure 2: Construction of the initial average grain for different stages of development. **a, c** Several individual grain models at stage 60 °DAA (**a**) and 310 °DAA (**c**); **b, d** Results of the initial average grain construction for each stage. Blue colors correspond to low variability, bright colors correspond to high variability (greater than 0.07 mm). Scale bar is 1 mm.

Acknowledgment

This research is supported by grants from INRA CEPIA and the financial assistance received from the region Pays de La Loire.

References

[1] N. Hughes, K. Askew, C. P. Scotson, K. Williams, C. Sauze, F. Corke, J. H. Doonan, and C. Nibau. Non-destructive, high-content analysis of wheat grain traits using x-ray micro computed tomography. *Plant Methods*, 13(1):76, 2017.

[2] T. D. Q. Le, C. Alvarado, C. Girousse, D. Legland, and A. Chateigner-Boutin. Use of x-ray micro computed tomography imaging to analyze the morphology of wheat grain through its development. Manuscript under review at Plant Methods journal.

[3] P. J. Besl and N. D. McKay. A method for registration of 3-d shapes. *IEEE Transactions on Pattern Analysis and Machine Intelligence*, 14(2):239–256, Feb 1992.

[4] Ian L. Dryden and Kanti V. Mardia. *Statistical Shape Analysis*. John Wiley & Sons, 1998.

[1]

Estimation of Leaf Color and Angle based on UAV-Captured Leaf-Scale Images for Indicator of Plant Growth

Kuniaki Uto [†1], Mauro Dalla Mura [‡1,2], Jocelyn Chanussot [§2,3], and Koichi Shinoda [¶1]

[1]Tokyo Tech World Research Hub Initiative (WRHI), School of Computing, Tokyo Institute of Technology, Tokyo, Japan
[2]Univ. Grenoble Alpes, CNRS, Grenoble INP, GIPSA-lab, Grenoble, France,
[3]Faculty of Electrical and Computer Engineering, University of Iceland, Reykjavik, Iceland

Abstract

Precision estimation of optical properties of leaves and angles of plants is necessary to evaluate the absorbed photosynthetically active radiation (APAR). However, this estimation from unmanned aerial vehicle(UAV)-captured leaf-scale images is a challenge.In this work, we propose a method based on tensor decomposition by which a set of images of leaves are decomposed into three terms, each of which related to the leaf normal, the sunlight direction and the leaf optical property, with multilinear rank-$(3, 3, 1)$.

Keywords: Aerial Leaf-Scale Image, Optical Property of Leaf, Leaf Angle, Direct/Diffuse Flux

1 Introduction

The structure of plant is an important factor in photosynthetic production because, given the photosynthetically active radiation (PAR) on a plant, the plant structure is related to the fraction of absorbed PAR (FAPAR) that determines the absorbed PAR (APAR). There is a linear relationships between net primary production (NPP) of a plant and APAR [1]. Among indices that represent plant structure, leaf area index (LAI), leaf angle distribution (LAD) and photosynthetic pigments contents are critical indices that make contributions to FAPAR. LAD determines plant interceptions of PAR inside the plants. PAR penetrates more deeply into the plants when leaf inclination angles are smaller, that results in more productivity [2].

With the era of UAV coming, the utility of aerial images for agricultural monitoring will be remarkably improved. One of potential application of UAV-captured images is phenotyping. LAD and optical properties of leaves are among the phenotypic traits. Compared with precision estimation of photosynthetic pigments contents based on laboratory spectral reflectance of leaves, retrieval of optical properties of leaves from aerial leaf-scale images of plant is challenging because there is shading in the leaf-scale images. The objective of this work is to retrieve optical properties of leaves and leaf angles from shading distribution in leaf-scale images of plants.

*This work was supported by JST PRESTO Grant Number JPMJPR17O2, Japan.

†Corresponding Author: uto@c.titech.ac.jp
‡mauro.dalla-mura@gipsa-lab.grenoble-inp.fr
§jocelyn.chanussot@gipsa-lab.grenoble-inp.fr
¶shinoda@c.titech.ac.jp

2 Methods

Our objective is to estimate leaf normals and optical properties of leaves based on leaf-scale images of plants. In this paper, we begin with a reflection model under clear sky in which direct sunlight is dominant. For the sake of simplicity of the optical model, we assume that plant leaves are Lambertian surface. Then, apparent reflectance of the leaf at x,t is given by

$$\rho(x,t,\lambda) = \mathbf{N}(x) \cdot \mathbf{L}(t)\ k'(\lambda), \tag{1}$$

where $k'(\lambda) = \frac{k(\lambda)}{\mathbf{N}_w \cdot \mathbf{L}_w\ \rho_w(\lambda)}$. $\mathbf{N}(x)$, $\mathbf{L}(t)$, $k(\lambda)$, $\mathbf{N}_w$, $\mathbf{L}_w$ and $\rho_w(\lambda)$ are the normal direction of leaf surface at a position x in image coordinates, a direction vector of direct sunlight at a time t, a Lambert coefficient of leaf surface at wavelength λ, the normal vector of the diffuse reference standard, a sunlight direction at the time of measurement and reflectance of diffuse reference standard at wavelength λ.

We define $\tau_{i,t} \in \mathbb{R}^{X_i \times B}$ as a two-dimensional data array of reflectance $\rho(x,t,\lambda)$ of a plant i at time t, where X_i and B are the number of pixels of the plant i and the number of bands, respectively. Given intraday time-series aerial images of agricultural field, we can utilize the temporal change in shading for estimating the spatial distribution of leaf surface normal directions. Let plant structures be invariant during intraday measurements. A stack of time-series images of a plant i, i.e., $\{\tau_{i,t}\}_{t=1}^{T}$, forms a three-dimensional structure spanned by spatial, spectral and temporal coordinates, i.e., $\tau_i \in \mathbb{R}^{X_i \times B \times T}$.

Let $N_i = (\mathbf{N}(x_1), \ldots, \mathbf{N}(x_{X_i}))^T \in \mathbb{R}^{X_i \times 3}$ and $\mathbf{L} = (\mathbf{L}(t_1), \ldots, \mathbf{L}(t_T))^T \in \mathbb{R}^{T \times 3}$ be matrices whose rows correspond to normal directions of surfaces at pixels $x_j,\ j \in \{1, \ldots, X_i\}$

Table 1: Averaged cosine similarities between leaf normals and estimations (unit: [deg]).

leaf angle	rotation angle			
	0	90	180	270
10	0.0374	0.0441	0.0206	0.3898
20	0.1315	0.5699	0.1194	0.4051
30	0.2597	0.8348	0.2365	0.2393
40	1.9954	0.2215	17.8133	0.1350

within the plant i, and illumination directions of direct sunlight $\mathbf{L}(t_j)$, $j \in \{1,\ldots,T\}$, i.e., L. As per equation (1), $\tau_{i,t}$ and τ_i can be decomposed into

$$\tau_{i,t} = (N_i L(t)^T) \circ \mathbf{k}'_i, \quad (2)$$

$$\tau_i = (N_i L^T) \circ \mathbf{k}'_i, \quad (3)$$

where the symbol $\circ$ represents the vector outer product. Given rank-3 matrices N_i and L and a rank-1 vector $\mathbf{k}'_i$, equation (3) is a decomposition into terms with multilinear rank-$(3,3,1)$.

The objective of tensor decomposition is to estimate intra-field variation of optical properties $\mathbf{k}'_i$ and normal directions of leaves N_i of individual plant $i \in \{1,\ldots,P\}$ based on aerial images $\{\tau_i\}_{i=1}^P$, where N is the number of plants. The tensor decomposition for estimating $\mathbf{k}'_i$ and N_i is defined by

$$\underset{\{N_i\}_{i=1}^P, L, \{\mathbf{k}'_i\}_{i=1}^P}{\operatorname{argmin}} \sum_{i=1}^{N} \|\tau_i - (N_i L^T) \circ \mathbf{k}'_i\|_F^2, \quad (4)$$
$$s.t. \;\; \mathbf{k}'_i \geq 0, \;\; \forall i \in \{1,\ldots,P\},$$

where $\|\cdots\|_F$ is a Frobenius norm and $\mathbf{k}'_i \geq 0$ means that all the elements of a vector $\mathbf{k}'_i$ are nonnegative. In this work, we used a solver based on optimization-based algorithm [3].

3 Experimental results

We applied the proposed tensor decomposition method to simulation data in which flat plates with 16 different angles were illuminated from 17 different solar angles. Given a horizontal plane is spanned by x (East-West) and y (North-South) axes, 4 flat planes whose angles between x axis and the planes were 10, 20, 30 and 40 degrees were generated. Then, the 4 planes were rotated by 0, 90, 180 and 270 degrees around z (zenith) axis. Consequently, flat planes with $4\times4 = 16$ different postures were generated. The 17 different solar angles correspond to every 30 minutes from 8:00 to 16:00 in May at a place in Europe. The Lambert coefficients of all the plates were identical (Fig. 1). Fig. 2 shows examples of changes of leaf colors with different sunlight angles.

Fig. 1 shows estimates of Lambert coefficients based on the simulated images. Table 1 shows averages of cosine similarities between leaf normals and estimations. The results demonstrate that proposed method successfully estimates leaf normals and Lambert coefficients with high accuracies.

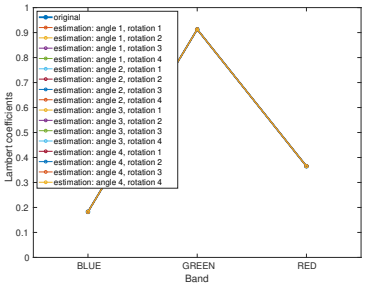

Figure 1: Lambert coefficients and estimations (angle (1,2,3,4) = (10, 20, 30, 40) [deg], rotation (1, 2, 3, 4) = (0, 90, 180, 270) [deg]).

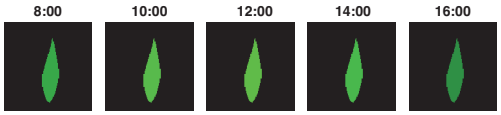

Figure 2: Simulated images.

4 Conclusion

We have proposed a novel method that estimates optical properties of leaves and angle based on shading distribution. The simulation results confirmed that the method successfully retrieved surface colors and angles when direct light is dominant and the targets are temporally stable.

References

[1] J. L. Monteith. Solar Radiation and Productivity in Tropical Ecosystems. *The Journal of Applied Ecology*, 9(3):747–766, 1972.

[2] S. K. Truong, R. F. McCormick, W. L. Rooney, and J. E Mullet. Harnessing Genetic Variation in Leaf Angle to Increase Productivity of Sorghum bicolor. *Genetics*, 201(3):1229 LP – 1238, nov 2015.

[3] N. Vervliet, O. Debals, and L. De Lathauwer. Tensorlab 3.0 - Numerical optimization strategies for large-scale constrained and coupled matrix/tensor factorization. In *Conference Record - Asilomar Conference on Signals, Systems and Computers*, 2017.

Green plant segmentation in hyperspectral images using SVM and hyper-hue

Huajian Liu, Brooke Bruning, Bettina Berger, Trevor Garnett

Australian Plant Phenomics Facility, The Plant Accelerator®, School of Agriculture, Food and Wine
University of Adelaide, Waite Campus
Building 32, Hartley Grove, Urrbrae, SA 5064
Corresponding author's Email: huajian.liu@adelaide.edu.au

Abstract

Green plant segmentation plays an import role in hyperspectral-based plant phenotyping, however, this topic is not given enough consideration. Existing image segmentation methods are dependent on data types, plants and backgrounds and might not utilise the power of hyperspectral data. We proposed a one-class support vector machine classifier combined with a pre-processing method named hyper-hue to segment green plant pixels in hyperspectral images. Experimental results showed that his method can segment green plants from backgrounds with fewer errors and therefore could be used as a general method for hyperspectral-based green plant segmentation.

Keywords: Hyperspectral image processing, Image segmentation, Plant phenotyping

1 Introduction

Hyperspectral imaging is a widely accepted and fast developing technology for plant phenotyping [1]. For most hyperspectral image analysis tasks, green plant segmentation is a necessary prerequisite which plays an import role for subsequent image processing procedures, however, the significance of this task is not well documented in current literature.

In the visible and near-infrared (VNIR) spectra, some vegetation indices developed for multispectral images, such as hue and normalized difference vegetation index (NDVI) [2], have been used, however, these indices did not take the advantages of the power of hyperspectral data for more accurate processing. In the range of short wavelength infrared (SWIR), the segmentation methods are application-dependent and there are no well-accepted procedures for reliable segmentation.

After an investigation of the most often used vegetation indices, hyperspectral image pre-processing methods and classifiers, this paper proposes an image segmentation method which uses the combination of hyper-hue [3] and one-class support vector machine (SVM) to segment green plants from the background in hyperspectral images. The method was tested using five different plant species in both VNIR and SWIR data and the experimental results showed that it can significantly reduce errors and could be adopted as a general approach for green plant segmentation in hyperspectral images.

2 Material and methods

Five plant species, including wheat (*Triticum aestivum*), barley (*Hordeum vulgare*), cotton (*Gossypium spp.*), arrowleaf clover (*Trifolium vesiculosum*) and Australian canary grass (*Phalaris aquatic*) were grown at The Plant Accelerator® (Australian Plant Phenomics Facility, University of Adelaide, Adelaide, Australia) in 2018. Each species has 70 to 200 pots. When the plants had enough leaves, the hyperspectral images were captured with a high-throughput WIWAM hyperspectral imaging system (WIWAM, Eeklo, Belgium). Two cameras were used to capture both of VNIR and SWIR images simultaneously in the dark chamber of the WIWAM system. The FX10 camera (Specim, Oulu, Finland) captured the VNIR data from 400 nm to 1000 nm with 1.3 nm bandwidth and the SWIR camera (Specim, Oulu, Finland) acquired data in the range of 1000 nm to 2600 nm with 5.7 nm bandwidth.

A classifier was trained and validated using a part of the data of wheat and then was tested using the independent data of the five plant species. In our initial study, after testing the well-accepted classifiers and pre-processing methods of hyperspectral data, we found that the supervised one-class SVM and hyper-hue outperform others. In VNIR or SWIR data, a one-class SVM was trained, validated and tested using the following steps. (1) The hyperspectral images were calibrated using Eq. (1),

$$r_{\mathrm{p}}(\lambda, x, y) = \frac{i_{\mathrm{p}}(\lambda, x, y) - i_{\mathrm{d}}(\lambda, x, y)}{\mathrm{i}_{\mathrm{w}}(\lambda, x, y) - i_{\mathrm{d}}(\lambda, x, y)} \quad (1)$$

where r_{p} is the reflectance values of the plant at the spatial location (x, y) and the wavelength λ. i_{p}, i_{d} and i_{w} represent the measured intensity values of plants, dark references and white references respectively. (2) The noisy bands with the wavelengths below 450 nm in the VNIR data and above 2400 nm in the SWIR data were removed. (3) 5000 pixels were selected manually and randomly from the top, middle and bottom parts of the wheat leaves in the 199 hyperspectral images of wheat, excluding the pixels on the borders of the leaves whose spectral signatures were the mixture of the leaves and backgrounds. Similarly, 2500 pixels of backgrounds were collected, including pots, bolt, soil, plastic, random noise, etc. 2500 pixels were randomly selected from the 5000 pixels of wheat as training data and the remaining 2500 pixels plus the 2500 pixels of backgrounds were used as validation data. (4) The data was transformed from the original space of hypercube to the space of hyper-hue [3] whose performance for material classification has previously been proven [4, 5]. (5) A one-class classifier of SVM with the radial basis function (RBF) kernel (python sklearn toolbox, svm.OneClassSVM) was trained and validated using the training and validation data. The parameters were tuned to get the optimized performance. The trained model is named HH in this paper. (6) The trained model was tested in hyperspectral images of different plant species which were independent of the training and validation data.

3 Experimental results and discussion

To evaluate the contribution of hyper-hue in step (4), another model which used similar training processes while ignoring step (4) was trained and the model is named REF in this paper. At first, the models were validated using the

validation data and the errors are listed in Table 1, in which FP, FN and MIS represent false positive rate, false negative rate and misclassification rate respectively. Table 1 shows that, compared with the REF method, the HH method can reduce the errors to the levels of lower orders. As explained by Liu, et al. [3], hyper-hue is independent of saturation and intensity and therefore it is less affected by unstable illumination from the angular deviation of local surfaces and self-shadows of plants. Also, hyper-hue could increase inter-class distance [4]. Next, the models were tested using hyperspectral images of wheat, barley, cotton, arrowleaf clover and Australian canary grass. For each species, a hyperspectral image which was independent of the training and validation data was randomly selected for testing. The images were firstly manually segmented using the Photoshop software and then were compared with the automatic segmentation. In the VNIR data, we compared several well-accepted vegetation indices, including NDVI, green normalized difference vegetative index (GNDVI), enhanced vegetation index (EVI) [6], etc. and found that the method using EVI with the threshold 0.3 can provide the best segmentation. The performances of the EVI, REF and HH methods were tested in the VNIR data while only the REF and HH methods were tested in the SWIR data. The misclassification rates are plotted in Figure 1 and Figure 2 and they show that the HH method significantly reduced the errors. Figure 3 shows the testing images of the REF and HH methods for the segmentation of barley in SWIR data.

Table 1 Error rates of SVM model validation

	VNIR			SWIR		
	FP	FN	MIS	FP	FN	MIS
REF	10.00%	0.32%	3.98%	0.20%	0.16%	0.18%
HH	0.00%	0.02%	0.02%	0.00%	0.04%	0.02%

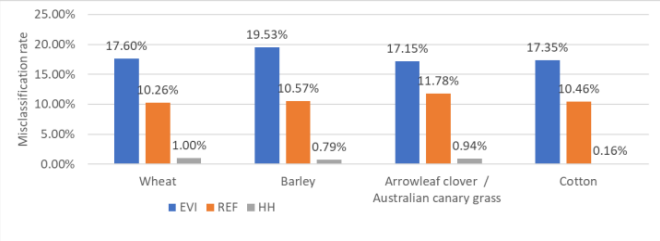

Figure 1 Misclassification rate in VNIR testing data

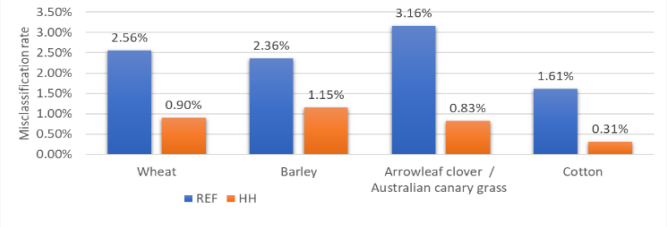

Figure 2 Misclassification rate in SWIR testing data

In the testing data, the error rates are higher than that in the validation data. There are several factors which could cause a higher error rate in the testing data. First, in the manual segmentation, the pixels on the borders of the leaves were classified as foreground while in automatic classification, these pixels could be classified as background since the spectral signatures of these pixels were the mixture of backgrounds and plants. Second, the manual segmentation could have errors, especially for the narrow-leaf plants of wheat and barley. The segmented images will be further processed to analysis the nutritional distribution in the plants, including nitrogen, phosphorous, etc. The accuracy of the segmentation can meet this requirement. Use larger training data to train more complex models, such artificial neural network (ANN) or deep-ANN, would obtain the same or better result, however, using a smaller data set to train a model with acceptable accuracy is preferred when labour and cost of data collection is concerned.

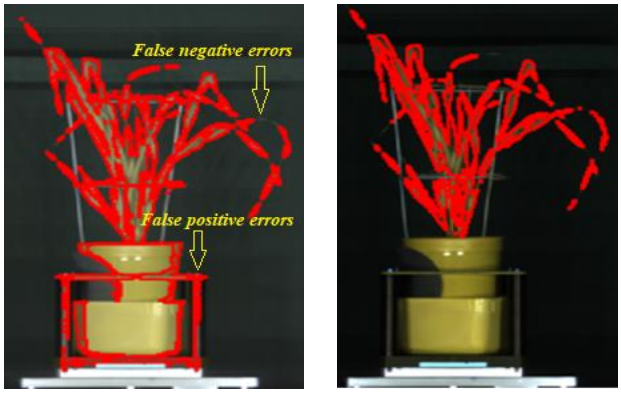

REF method HH method

Figure 3 Testing images of the REF and HH method for the segmentation of barley in SWIR data (the red colour marks the contours of the plants)

4 Conclusion

Green plant segmentation in hyperspectral images is important for plant phenotyping. This paper introduces a segmentation method which uses the combination of SVM and hyper-hue[1]. Experimental results showed that this method outperformed the approaches using vegetation indices or SVM only. The model was trained using the data of wheat and worked equally well for other species. The modelling method was suitable for both VNIR and SWIR data. In the future, this green plant segmentation method will be further tested using data collected in the field, such as on aircrafts or ground-based vehicles.

References

[1] U. Seiffert, F. Bollenbeck, H. Mock and A. Matros, "Clustering of crop phenotypes by means of hyperspectral signatures using artificial neural networks", in *2nd Workshop on Hyperspectral Image and Signal Processing: Evolution in Remote Sensing (WHISPERS), 2010 2nd Workshop*, 2010, pp. 1-4, doi: 10.1109/WHISPERS.2010.5594947.

[2] H. Liu, S. H. Lee and C. Saunders, "Development of a machine vision system for weed detection during both off-season and in-season in broadacre no-tillage cropping lands", *American Journal of Agricultural and Biological Sciences,* vol. 9, pp. 174-193, 2014, doi: 10.3844/ajabssp.2014.174.193.

[3] H. Liu, S. H. Lee and J. S. Chahl, "Transformation of a high-dimensional color space for material classification", *Journal of the Optical Society of America A,* vol. 34, pp. 523-532, 2017, doi: 10.1364/josaa.34.000523.

[4] H. Liu and J. S. Chah, "A multispectral machine vision system for invertebrate detection on green leaves ", *Computer and Elecronics in Agriculture,* vol. 150, pp. 279-288, 2018, doi: https://doi.org/10.1016/j.compag.2018.05.002.

[5] H. Liu, S. H. Lee and J. S. Chahl, "A multispectral 3D vision system for invertebrate detection on crops", *IEEE Sensors* pp. 1-14, 2017, doi: 10.1109/JSEN.2017.2757049.

[6] A. Huete, K. Didan, T. Miura, E. Rodriguez, X. Gao and L. Ferreira, "Overview of the radiometric and biophysical performance of the MODIS vegetation indices", *Remote Sensing of Environment,* vol. 83, pp. 195-213, 2002, doi: 10.1016/S0034-4257(02)00096-2.

[1]The hyper-hue algorithm is free to download from https://github.com/Harwis/HC2HHSI_python or https://github.com/Harwis/HC2HHSI

Evaluation of the Data Distillation strategy for a better generalization of convolutional neural networks in plant phenotyping. A study case on wheat ears detection

Etienne David[1], Raul Lopez-Lozano[1], Simon Madec[1], Benoit De Solan[2] and Frédéric Baret[1]

[1] INRA UMR 114 EMMAH, UMT CAPTE, Domaine Saint-Paul, Site Agroparc, F-84914 Avignon, France
[2] ARVALIS, 3 Rue Joseph et Marie Hackin, 75116, France

Abstract

Convolutional neural networks (CNN) have shown great interest for plants and organ counting. However, the accuracy of CNN to yield unbiased results on unseen data is determined by the domain dependence of the training datasets. In this study, an approach called Data Distillation to solve the problem of domain shift is evaluated in a study case to detect wheat ears from RGB images. The training and test datasets correspond to two different experimental sites. We demonstrate that Data distillation divides by 3 the error in the estimation of ears density. These results are promising to improve invariance on acquisitions conditions.

Keywords: Deep Learning, Field phenotyping, Remote Sensing, Ear counting.

1 Introduction

The development of high-throughput phenotyping platforms has open new avenues to characterize plant functioning. The important availability of optical data –e.g. in the form of RGB or multispectral images, point clouds from LiDAR data– in those platforms requires the use of automatic approaches to extract relevant information of plant or canopy structure (e.g. structural traits like the amount of leaf area, the density of plants and plant organs). The use of deep learning algorithms, and, more specifically, convolutional neural networks (CNN), has become very popular in plant phenotyping. It has proven to be efficient in determining several structural traits in fully automatic manner such as plant counting [1], detecting the presence and estimating the density of reproductive organs [2], or identifying individual crops [3]

Despite these important advantages, the empirical nature and complexity of deep learning often make difficult to understand how the variability of image features may condition the reliability of a trained CNN applied on unseen data. Even under similar acquisition set-up environments – e.g. same camera, same measurement protocol– the operational use of CNNs to solve object detection/counting problems in phenotyping experiments exhibit some dependence of the domain when applied to dataset outside the training set:

- Image acquisition parameters such as spatial resolution, blur, and integration time.
- Agronomic variability, such as morphological differences across genotypes, or variability on plant phenology.
- Environmental factors, such as illumination condition and soil background properties.

A strategy to solve this domain shift problem is critical to improve the robustness of Deep Learning algorithms in plant phenotyping. In this paper, we explore the idea of Data distillation, introduced by [4]. Data distillation identifies automatically those favorable unlabeled observations in the target domain that help to improve the generalization of a previously trained CNN. This paper explains and evaluates the implementation of Data Distillation in the detection of wheat ears over different datasets of RGB images from phenotyping experiments.

2 Material and methods

a. Data acquisition

RGB Images on wheat canopies were acquired after the flowering stage using a Sony ILCE-6000 RGB camera fixed on a boom and oriented at nadir, in two different experiments in the south of France: Gréoux (N 43° 45', E 5° 53') and Mons (N 50°27', E 3° 57'). The images were splitted into a training dataset (239 images, corresponding to the three different dates acquired at Gréoux), and testing dataset (182 images, corresponding to one dates at Mons). The images measure 6000 pixels by 4000 pixels. Each one represents a microplot. A set of 34 patches of 512 pixels per 512 pixels is cropped for each of them. The images were

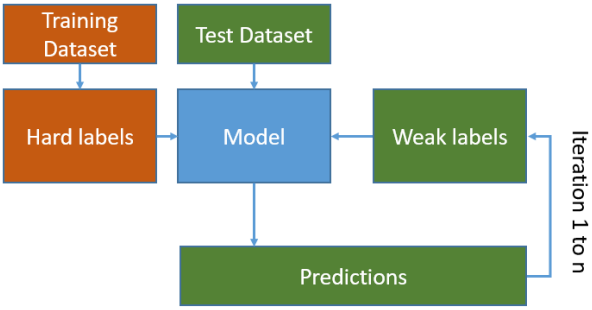

Figure 1: Schema of training using Data Distillation strategy

labelled manually, identifying the wheat ears present in the image. Ears density from the images is calculated by dividing the number of ears detected in each microplot by the ground area covered by the images. Additionally, ears density was manually determined in the experimental field by experts counting the number of ears on each microplot.

b. Domain adaptation through Data Distillation

Faster RCNN detection model [5] was used to detect ears in the images. The model was pre-trained on the MS COCO Dataset and trained with the mmdetection toolbox using the training dataset with a batch size of 4 images. Convergence was verified within 10 epochs.

Data distillation is an iterative re-training process that incorporates automatically information from the test dataset to improve the generalization of the model (Figure 1). At iteration 0, the Faster RCNN is trained only with the images of the training dataset. In successive iterations, bounding boxes are predicted from unlabeled images of the test dataset, and multiple affine transformations (rotation, flipping, zoom) are applied to generate image ensembles. The Faster RCNN from the previous iteration is applied over the transformed images and ensemble predictions are merged into a single prediction with the non-max suppression algorithm. The predictions with a score above 0.5 –i.e. a priori, those observations from the test dataset with more chances to be well classified– are identified as "weak labels", and used as input to re-train the network, merging them with the original training set. The ratio between hard and weak labels is 75%/25% to avoid a decrease of the network performance. This process is repeated until performance started to decrease. To evaluate our approach, we calculate the relative Root Mean Square Error between the predicted number of ears and the ground truth.

3 Results and discussion

At iteration 0 corresponding to the network trained with data from a single site, the relative Root Mean Square Error (rRMSE) is large (Figure 2). This is mainly a consequence of contrasted illumination conditions between the Gréoux and Mons experiments, visually appreciable in the original RGB images. Data distillation allows to decrease

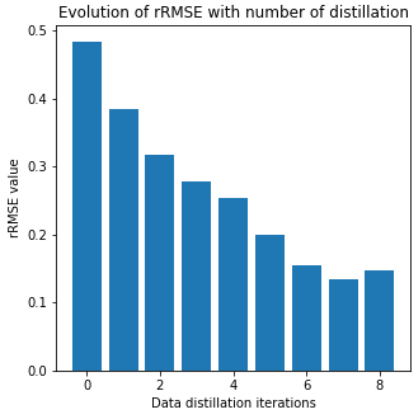

Figure 2: Relative RMSE on counting error against ground measurement depending on the number of Data Distillation

dramatically the relative error, reducing the rRMSE by almost three at iteration 7 (Figure 2). However, the rRMSE starts to increase at iteration 8. The generation of weak labels from predictions don't prevent apparition of false positives which led to a decrease in performance. From iteration 8, the performances continue to decrease.

4 Conclusion

This approach demonstrates the potentials of data distillation to overcome the domain shift between the data labelled available for training and the diversity existing in phenotyping experiments, which is highly relevant in those experiments where the variability of available domains for network training is low. Nevertheless, further efforts are necessary to identify an appropriate method to select efficiently weak labels, thus avoiding an eventual decrease of the performance after many iterations.

5 References

[1] Aich, Shubhra, et al. "Deepwheat: Estimating phenotypic traits from images of crops using deep learning." 2018 IEEE Winter Conference on Applications of Computer Vision (WACV). Vol. 3. 2018.

[2] Madec, Simon, et al. "Ear density estimation from high resolution RGB imagery using deep learning technique." Agricultural and Forest Meteorology 264 (2019): 225-234.

[3] Jin, Shichao, et al. "Deep learning: individual maize segmentation from terrestrial lidar data using faster R-CNN and regional growth algorithms." Frontiers in plant science 9 (2018): 866.

[4] Radosavovic, Ilija, et al. "Data distillation: Towards omni-supervised learning." Proceedings of the IEEE Conference on Computer Vision and Pattern Recognition. 2018.

[5] Girshick, Ross. "Fast r-cnn." Proceedings of the IEEE international conference on computer vision. 2015

Ripe and unripe raspberry segmentation using u-nets

Dominic Williams[1], Avril Britten[1], Alison Karley[2], Susan McCallum[2] and Julie Graham[2]

[1]James Hutton Limited, Dundee, Scotland
[2]James Hutton Institute, Dundee, Scotland

Abstract

We present an image segmentation method aimed at detecting raspberry fruit on a plant and determining if that fruit is ripe or unripe. We use images of entire raspberry plants grown in field conditions for this task. A deep learning framework based on u-nets with a resnet-34 backbone is used for this task. We achieve good precision and recall of ripe and unripe fruit with f1 score of 0.884 for ripe berries and 0.868 for unripe berries.

Keywords: Plant Imaging, Image Segmentation, Phenotyping, Field Imaging

1 Introduction

One of the most important traits for plant phenotyping is yield. The central aim of growers is to produce as much yield as possible with minimum input costs. Accurately measuring yield in the field is therefore important to allow accurate predictions for supply chains. For soft fruit crops fruit picking is a major expense to the business requiring large amounts of manual labour. This issue is also relevant to researchers studying crops as picking all experimental fruit can significantly add to project costs.

One of the other challenges related to fruit is scheduling pickers to pick fruit when they are at optimal ripeness. This means that measuring both the amount of already ripe fruit and any unripe fruit that may be picked in a few weeks' time is important for growers and also researchers. As the fruit ripens the colour changes, enabling this to be tracked using imaging. This also produces challenges for accurate segmentation of the fruit especially early green fruit which is hard to distinguish from plant leaves and shoots.

This study investigated using imaging by standard colour digital photography to locate and segment both ripe and unripe berries. This has uses both as a tool in its own right and as an additional tool to support a hyperspectral imaging platform[1] for high throughput phenotyping that we are currently developing.

2 Related work

There have been several previous studies aimed at automated fruit detection by use of imaging. Previous work by the authors has segmented ripe raspberries from hyperspectral images using a colour based threshold to detect red pixels. This method is unable to detect unripe fruit in the green stage of development as is similar colour to plant leaves.

Early work looking at the problem of fruit detection has used a variety of handcrafted features to solve specific fruit detection works [2]. More recently there have been a few approaches using deep learning methods to tackle to problem. These have treated the problem as either a semantic segmentation problem [3] or as an instance segmentation problem [4].

There have been several studies using a variety of deep learning methods to solve plant imaging problems. A group in Nottingham used stacked hourglass method to accurately locate wheat kernels and leaf tips [5]. They used point-based annotations with single clicks on objects of interested then generated heat maps from these points which were fed into stacked hour glass network. This approach achieved good accuracy in locating points after applying some post processing to the generated heat maps.

Our work builds on this study by similarly generating heat maps from single point clicks marking the fruit. We have replaced the stacked hour glass network with a u-net. U-nets have been widely used for sematic segmentation where the desired output is an image of similar dimensionality to the original image.

3 Method

Images of raspberry plants were taken using a Cannon PowerShot SX60 camera. Images were taken on raspberry plants grown in field conditions in Invergowrie, Scotland. The photos used in this study were all taken on a single date 18th July 2018 at a time when the majority of the fruit on the bushes was ripe but both ripe and unripe fruit was present. The images were taken to include a single entire bush in each image. A total of 236 images of different bushes were used for model training and validation. A 20:80 split was used between training and validation data sets. A second set of 33 images were used as a test set.

The images were annotated manually by first going through and clicking on all ripe fruit, then a second pass through the images clicked on all unripe fruit.

Figure 1: Left tile of image containing both ripe and unripe fruit. Right corresponding distance map tile derived from manual marking.

The images were then split into tiles of approximate 500x500 pixels each. For each tile an original rgb image was paired with a distance map with different colour channels being used to represent ripe and unripe fruit. An example of image distance map is shown in figure 1 above.

We chose to use a u-net network with a resnet-34 based architecture, pretrained on image-net, for our neural network. U-net's have been widely used for image to image problems after their introduction for biomedical image segmentation [6]. The network was first trained on 128x128 images, then further refined on 256x256 images before final training was carried out at 400x400 tiles. All steps involved a reduction in size based on original image sizes.

This progressive resizing allowed for the network to be trained quickly on smaller images and then further improved on larger images. Similar results were achieved using 256 and 400 sized images indicating trying full sized images may not have resulted in any further improvement.

In order to go from the output heat maps back to locations of fruit a local maxima transformation was used. First a threshold was applied to the images to remove very small peaks found in back ground areas. Then a local maximum filter was applied to find any points that were a local maximum excluding peaks within 20 pixels on other peaks. The points found were then compared to the original annotations. Any points within a similar distance of 20 pixels were considered to be marking the same fruit. Precision and recall were then calculated for all the images in the test set for both ripe and unripe berries based.

4 Results and Discussion

For evaluation a separate test set of images was used. This was done as the performance of validation set was used in making decisions on learning rate and when to change image resolution so model may have been some way optimised for validation set. These images were taken at the same time as original set, but manual annotation happened at a later time compared to initial annotation.

At maximum resolution tested 400x400 a F1 score for ripe berry detection of 0.884 was achieved for unripe berries the score was 0.868. This was only a slight improvement on scores of 0.883 and 0.832 achieved at a 256x256 resolution. The lack of improvement shown between 256 and 400 sized images indicates that the lower resolution is probably sufficient for the task.

Figure 2: Example images with ripe and unripe fruit marked. Circles are output from network stars from manual annotation.

The method was able to successfully ignore distant berries on plants occurring in rows behind the plants. This is probably due to the network learning something about the required size of berries to find.

The network struggled with clusters of berries close together where distinguishing individual berries becomes more challenging. This may be due to the fact the method we used is best suited to sematic segmentation tasks however methods designed for instance segmentation also struggle with the task of distinguishing objects of same class that occlude each other.

We have presented a method that is able to detect ripe and unripe raspberries from images taken of raspberry plants in the field. This shows that methods developed on images acquired in a controlled environment can be adapted for use in the field.

References

1. Williams, D., et al., *A method for automatic segmentation and splitting of hyperspectral images of raspberry plants collected in field conditions*. Plant Methods, 2017. **13**(1): p. 74.
2. R. Jiménez, A., R. Ceres, and J. L. Pons, *A Survey Of Computer Vision Methods for Locating Fruit on Trees*. Transactions of the ASAE, 2000. **43**(6): p. 1911-1920.
3. Dias, P.A., A. Tabb, and H. Medeiros, *Multispecies Fruit Flower Detection Using a Refined Semantic Segmentation Network*. IEEE Robotics and Automation Letters, 2018. **3**(4): p. 3003-3010.
4. W. Chen, S., et al., *Counting Apples and Oranges with Deep Learning: A Data Driven Approach*. Vol. PP. 2017. 1-1.
5. Pound, M.P., et al. *Deep learning for multi-task plant phenotyping*, IEEE Int. Conf. Comput. Vis. (2017).
6. Ronneberger, O., P. Fischer, and T. Brox. *U-net: Convolutional networks for biomedical image segmentation*. in *International Conference on Medical image computing and computer-assisted intervention*. 2015. Springer.

Combining Computer Vision and Deep Learning for High-Throughput Aerial Phenotypic Analysis in Wheat Pre-Breeding

Alan Bauer[1,+], Joshua Ball[1,+], Joshua Colmer[1], Simon Orford[2], Simon Griffiths[2], Ji Zhou[1,3,4,*]

[1]Earlham Institute, [2]John Innes Centre, [3]University of East Anglia, Norwich Research Park, UK
[2]Plant Phenomics Research Center, Nanjing Agricultural University, Nanjing, China

Abstract

In this article, we introduce an automated analysis pipeline that combines modern computer vision (CV) and deep learning (DL) for large-scale aerial phenotypic analysis in wheat pre-breeding. The pipeline contains a customized DL classifier to segment hundreds of wheat plots in field conditions, as well as CV algorithms to improve the segmentation result. After that, plot-level phenotypic analysis algorithms have been developed in the pipeline to measure canopy traits during key growth stages.

Keywords: Aerial phenotyping; deep learning; image analysis; phenotypic analysis; wheat.

1 Introduction

Aerial imagery has been popularly used in crop phenotyping in recent years, an approach that is capable of collecting large in-field crop images during the growing season. To extract meaningful phenotypic information from image data, high-throughput analytic algorithms are required to measure traits such as vegetative indices and canopy structure [1]. In cereal breeding, aerial imagery has been used to monitor key yield-related traits and crop performance in field conditions, based on which reliable decisions can be made to select lines that are likely to increase yield and yield stability [2].

While a great deal of aerial image data can be collected every day, it is technically difficult to analyze the acquired datasets in a high-throughput and reliable manner [3]. In order to address this challenge, we have been developing automated analysis pipelines for aerial phenotyping since 2016 [4]. By combining CV and DL with modular software design, we have established an aerial image analytic platform that embeds a trained DL classifier (*i.e.* a convolutional neural network, CNN [5]) to segment hundreds of wheat plots in field experiments, as well as CV algorithms to rectify the segmentation. This article reports the analysis platform and its application to a wheat pre-breeding experiment conducted in 2016, at the Norwich Research Park, UK.

2 UAV-Based Aerial Phenotyping

Aerial imaging was conducted using an unmanned aerial vehicle (UAV), DJI Phantom 3 Pro, which is easy-to-operate and easy-to-access. Two approaches were followed in aerial phenotyping: (1) the standard DJI Go app to fly the UAV to high altitudes (*e.g.* 60 meters) to acquire images for the entire field; (2) the Pix4D Capture app to fly a programmed mission to cover the field at lower altitudes (*e.g.* 10 meters). Both applications allow the pilot to plan grid-based flights, drone speed, image overlap (the front and back overlap is at least 80% and a side overlap is 70% minimum), camera angles, and altitudes. Because lower-altitude flights can retain detailed canopy information, most of our flights were carried out at lower altitudes. Hundreds of images were then 'stitched' to create a large orthomosaic image via the Pix4Dmapper software, representing wheat vegetation and canopy information of the entire experiment field.

3 Deep Learning and Segmentation

We chose DL for plot segmentation after a number of attempts using CV approaches. Because different wheat genotypes change color dissimilarly throughout the season, it is challenging to design a method to segment hundreds of wheat plots in a dynamic manner. As a result, a combined approach has been chosen in our work.

To carry out phenotypic analysis of each plot, we firstly segmented soils in a given aerial image using a trained CNN model (Fig. 1). The architecture follows the AlexNet [6]. A

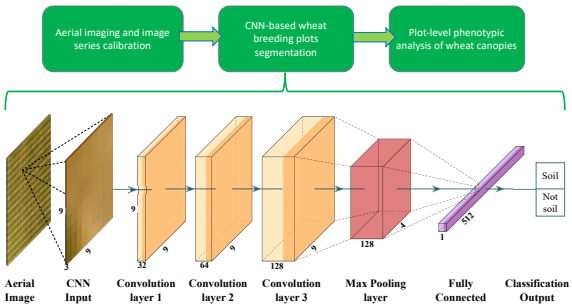

Figure 1: The CNN architecture and the analysis workflow

simple CNN classifier was established that contains three consecutive convolutional layers, followed by max pooling and fully connected layers, as well as batch normalization and drop out layers to prevent overfitting [7].

Because of the limited changes of features in the soil (*i.e.* color and pattern) during key growth stages, we trained the CNN model with over 6,000 labelled soil images using the 2016 aerial image series. The training datasets were selected across key growth stages to improve the generalization of the classifier. A 9x9 pixel sliding window is used to classify soil or non-soil regions with a step size of 6, *i.e.* each sub-image is verified around three times. A sub-image must obtain a soft-max output of at least 0.98 before it can be classified as soil. This threshold was optimized to reduce false positives under crop scientists' verification.

4 Automated Phenotypic Analysis

After training the CNN classifier, we applied the model to a series of 15 aerial images collected between 28th April and 29th July 2016, for a pre-breeding experiment that contains 784 six-meter wheat plots (Fig. 2A). Because the CNN method produces a noisy binary mask of soil signals (Fig. 2B), we therefore applied CV algorithms to improve the soil segmentation mask. A Hough Transforms method [8] has been applied to determine horizontal and vertical lines so that the field layout could be reconstructed. Then, each plot was measured independently and treated as an individual object so that it could be extracted from the field image and placed in a comprehensive matrix for phenotypic analysis.

In Figure 2C, each column in the matrix denotes a given plot (*i.e.* a specific genotype) and how it performed during key growth stages; whereas each row in the matrix denotes the date of the aerial imaging together with the visual representation of all plots monitored on the day. After arranging the plots according to genotypes and phenotyping dates, we finally conducted trait analysis of each plot by computing indices such as Excess Red (ExR), normalized greenness, and an improved vegetative index (*i.e.* Excess Green, ExG, minus ExR, ExG-ExR) [9] based on red and green channels of the plot-level images (Fig. 2D). These indices are popularly used in the identification of plant biomass, ecological assessments, and crop vegetation. For example, ExR values (colored red) increased steadily after

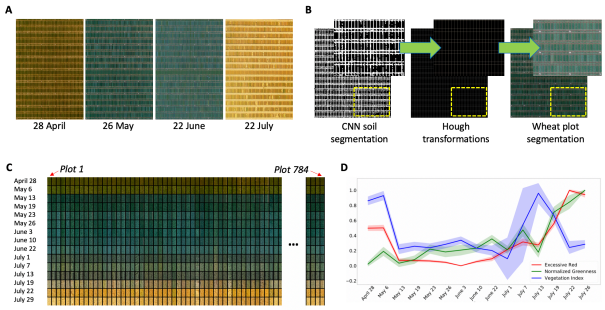

Figure 2: Phenotypic analysis and plot level vegetative indices

the anthesis (10th June), correlating with the increase of biomass of wheat canopy due to grain filling. Normalised greenness dropped after grain filling (7th July), indicating the start of ripening. The improved vegetative index (*i.e.* ExG-ExR) values changed dramatically among key growth stages (*e.g.* from heading to flowering, 6th May), showing the change of key growth stages described before [9].

5 Conclusion

A major advantage of aerial phenotyping over ground-based methods is the increase in throughput and scale [10]. In our work, we used weekly flights to cover key growth stages, based on which phenotypic analysis of plot-level vegetative indices and canopy information can be recorded. We have extended the analysis platform to monitor canopy structure and interactions between genotypes and environment, for which we will report in subsequent publications.

Acknowledgement

The authors would like to thank researchers at JIC, as well as all members of the Zhou laboratory at EI and NAU for fruitful discussions.

References

[1] Sadegi-Tehran P. *et al.* Multi-feature machine learning model for automatic segmentation of green fractional vegetation cover for high-throughput field phenotyping. *Plant Methods*. 13:1–16, 2017.

[2] Reynolds M. and Langridge P. Physiological breeding. *Curr Opin Plant Biol*. 31:162–71, 2016.

[3] Tardieu F. *et al*. Plant Phenomics, From Sensors to Knowledge. *Curr Biol.* 27:770–83, 2017.

[4] Bauer A. *et al.* AirSurf-Lettuce: an aerial image analysis platform for ultra-scale field phenotyping and precision agriculture using computer vision and deep learning. *bioRxiv*. 2019.

[5] Alex K. *et al*. ImageNet Classification with Deep Convolutional Neural Networks. *Neural Information Processing Systems*: 1097–1105, 2012.

[6] Krizhevsky A. *et al*. Alexnet. *Adv Neural Inf Process Syst*: 1–9, 2012.

[7] Ioffe S. & Szegedy C. Batch Normalization: Accelerating Deep Network Training by Reducing Internal Covariate Shift. *arXiv*, 2015.

[8] Dida R.O. Use of the Hough transformation to detect lines and curves in pictures. *Mag Commun ACM*. 15:17–22, 1972.

[9] Meyer G.E. and Neto JC. Verification of color vegetation indices for automated crop imaging applications. *Comput Electron Agric*. 63:282–93, 2008.

[10] Reynolds D. *et al*. What is cost-efficient phenotyping? Optimizing costs for different scenarios. *Plant Science*, 282:14–22, 2018.

The P2S2 segmentation dataset: annotated in-field multi-crop RGB images acquired under various conditions

Simon Madec[1], Kamran Ifran[1], Etienne David[1,2], Kaaviya Velumani[1,3], Gaetan Daubige[2], Jeremy Labrosse[3] , Wei Guo[4],Marie Weiss[1], Frederic Baret[1]

[1]INRA, UMT-CAPTE, EMMAH UMR1114, Avignon, France
[2]Arvalis, Avignon, France
[3]Hiphen SAS, Avignon, France
[4]The University of Tokyo · Japan

Abstract

Images play a vital role in crop phenotyping. Pixel-wise classification (into vegetation/background) or semantic segmentation is a critical step in the computation of several canopy state variables. Current state of the art methodologies based on convolutional neural networks are trained on data acquired under controlled environments. These models are unable to generalize to real-world dataset and hence need to be fine-tuned using new labels. This motivated us to create the P2S2 segmentation dataset – a collection of multi-crop RGB images from different acquisition conditions. We present here the dataset and state of the art results.

Keywords: Dataset, Segmentation, Convolutional Neural Networks, RGB, Crop

1 Introduction

Deep learning and convolutional neural networks (CNNs) have recently demonstrated their huge potential in plant image segmentation [1]. However, the training and validation images are often acquired in laboratory and under controlled illumination conditions [2]–[3]. The evaluation of the method performances is also often limited to specific conditions including species or cultivars, crop stage, and illumination conditions. To overcome this issue, we propose the P2S2 dataset of annotated images: it was initially acquired for the validation of vegetation products derived from the Sentinel 2 satellite. It is composed of 75 images acquired over nine crops and different stages/conditions. We first describe our annotation strategy to build an accurate dataset. We then use the P2S2 segmentation dataset to evaluate the performances of a CNN trained with already existing datasets from the literature. We hope that this publicly available dataset will help crop phenotyping research to overcome the bottleneck in robust segmentation model building.

2 Materials and methods

2.1 Image collection: The data collection was carried out in four sites in France and Belgium chosen for their varied climatic and soil conditions. These four sites were cultivated with nine crop species - wheat, rapeseed, maize, sunflower, sugar beet, rice, potato, soybean and grassland. We considered five acquisition dates across the growing season in such a way to cover as many growth stages as possible. Downward looking digital RGB images were acquired at the ground level. Approximately 2400 images of size 6000 x 4000 pixels were collected through this experiment with a spatial resolution of 0.2mm. From these images, we picked up 20 random patches of 512 x 512 pixels for each crop species. A maximum of four patches before and after the appearance of organs was selected. This led to a total of 75 images

2.2 Annotation strategy: Thirteen experts precisely annotated the 75 images using a custom improved version of the JavaScript annotation tool provided by [4]. To avoid annotation bias due to subjectivity, at least two independent experts reviewed each annotated image. The dataset was annotated following a simple rule: labeling all the pixels belonging to a plant as vegetation (including flowers, spikes, and dried leaves) and the rest as background.

Figure 1 Examples of images and their corresponding annotated masks

2.3 CNN architecture:

We built a CNN inspired from the U-Net convolution-deconvolution architecture. We used ResNet with 18 layers, initialized on the ImageNet dataset, as the backbone architecture. The training dataset was composed of five ready-to-use datasets that included the images and their corresponding vegetation/background mask. These datasets correspond to a range of vegetation: CVPP dataset (top view of rosette plants), Easy-PCC (rice and wheat fields), wheat, carrot and weeds, and one other dataset of wheat (unpublished) [5]–[7]. This constituted 1400 images, from which 15% was withheld for validation.

2.4 Evaluation metrics:

The CNN model was tested on the P2S2 segmentation dataset and its performances were also compared with a random forest (RF) model. The RF classifier was trained with the RGB pixel values, and we used 100 trees in the final estimator parameters. The fraction of vegetation and the mean IOU from these two approaches were compared.

3 Results and Discussion

3.1 CNNs achieve comparable performance to RF:

Both approaches achieved a relative error of 20% on the P2S2 dataset. The lowest performances were achieved on crop species that were not selected in the training database. For the CNN, the performances are affected by the spatial resolution and the sharpness of the images. Regarding the RF model, the main limitations are due to strong illumination conditions, soil appearance and the presence of non-green vegetation.

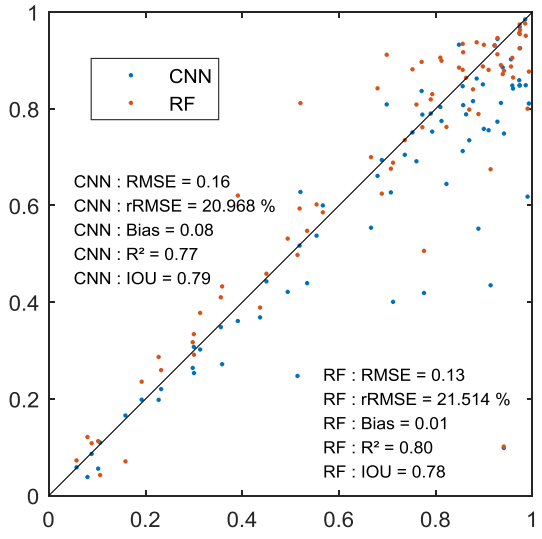

Figure 2: Vegetation cover estimates by CNN and RF

4 Conclusion and Perspective

We introduced a new, carefully annotated, precise, diverse image dataset acquired in a realistic environment. This challenging dataset is designed to improve the segmentation of vegetation images by building robust models. Moreover, it could be used as a common benchmark for future studies on vegetation segmentation It was used to evaluate a CNN approach trained on existing datasets from the literature. Results showed quite poor performances of this method due to the discrepancies between the training and the P2S2 dataset.This highlights the overall-value of this new dataset. Future work will focus on data augmentation and domain adaptation.

Acknowledgement

We acknowledge the financial support of the Centre National d'Etudes Spatiales (CNES) through a research grant under the program TOSCA (Terre solide, Océan, Surfaces Continentales, Atmosphère) for the acquisition of in situ measurements. We are also very grateful to the participants of the in situ measurements over the different sites.

References

[1] H. Scharr *et al*., "Leaf segmentation in plant phenotyping: a collation study," *Mach. Vis. Appl*., vol. 27, no. 4, pp. 585–606, 2016.

[2] P. Lottes, J. Behley, A. Milioto, and C. Stachniss, "Fully Convolutional Networks with Sequential Information for Robust Crop and Weed Detection in Precision Farming," *ArXiv Prepr. ArXiv180603412*, 2018.

[3] J. R. Ubbens and I. Stavness, "Deep Plant Phenomics: A Deep Learning Platform for Complex Plant Phenotyping Tasks," *Front. Plant Sci*., vol. 8, 2017.

[4] P. Tangseng, Z. Wu, and K. Yamaguchi, "Looking at outfit to parse clothing," *ArXiv Prepr. ArXiv170301386*, 2017.

[5] H. Scharr, M. Minervini, A. Fischbach, and S. A. Tsaftaris, "Annotated image datasets of rosette plants," 2014.

[6] W. Guo, B. Zheng, T. Duan, T. Fukatsu, S. Chapman, and S. Ninomiya, "EasyPCC: Benchmark Datasets and Tools for High-Throughput Measurement of the Plant Canopy Coverage Ratio under Field Conditions," *Sensors*, vol. 17, no. 4, Apr. 2017.

[7] S. Haug and J. Ostermann, "A crop/weed field image dataset for the evaluation of computer vision based precision agriculture tasks," in *European Conference on Computer Vision*, 2014, pp. 105–116.

Daily high resolution RGB images allow accurate dating of heading stage in wheat crops

Kaaviya Velumani[1], Simon Madec[2], Jeremy Labrosse[1], Jocelyn Gillet[1], Raul Lopez Lozano[2], Benoit de Solan[3], Frederic Baret[2]

[1]Hiphen SAS, Avignon, France
[2]INRA, UMT-CAPTE, EMMA-PACA, Avignon, France
[3]Arvalis Vegetal, Avignon, France

Abstract

Heading is a critical phenological stage that constitutes the transition between vegetative to reproductive phases of wheat during which the plant becomes highly sensitive to abiotic stress. Observations of heading stage are currently done visually by operators in the field. In this study, we present a Convolutional Neural Network (CNN)-based methodology to estimate automatically the heading date from daily images taken by a network of 27 field sensors. The results provided by this methodology have an absolute mean error of 1.58 days over 21 sites and are validated against expert observations.

Keywords: Heading Date, Internet of Things for Agriculture, CNN, Phenology

1 Introduction

Accurate observations of the wheat heading date are essential within breeding programs and decision-making in farms to optimize yield and quality during the grain filling stage. Very few attempts exist to determine the date of heading automatically. The work of [1] proposing a CNN-based method for the discrimination of phenological stages of wheat, seems promising, but so far, no results on the absolute accuracy of the method are provided. In this study, we present a methodology to estimate automatically the heading date from daily images taken by a sensor located in agricultural fields. To achieve this, a CNN is first trained to detect wheat ears on individual images and the heading date is determined by the evolution of the ears present in the daily images along the growing season.

2 Materials and methods

2.1 Field campaigns: Field observation systems[1], named Internet of Things for Agriculture (IoTA), developed by Bosch and Hiphen, were installed in 27 fields across France, sown with 8 varieties of soft (Triticum Aestivum) and durum (Triticum Durum) cultivars. They collected data throughout the 2017 and 2018 growing seasons. This includes daily RGB images taken 1m above the crop canopy, with a horizontal field of view of 55°, having dimensions of 1024 x 768 pixels and footprint of ~10.8 m^2.

2.2 Visual determination of the heading date: The heading date is defined as the time when 50% of the final number of ears have emerged from the base of the flag leaf by 50% of their length [2]. A group of experts determined the heading date on the fields monitored by analyzing the time series images from the IoTAs.

2.3 Automatic detection of wheat ears in RGB images: The daily images from 6 field sensors were divided into three groups: training, hyper-parameter tuning (to determine the learning rate decay, number of epochs, batch size and dropout percentages) and test (as shown in Table 1). Each image within these groups was then split into patches of 256 x 256 pixels with 50% overlap to prevent GPU memory problems and limit border effects. These patches were visually attributed to the class "headed" or "not headed" as shown in Figure 1. Inception-ResnetV2 network [3], pre-trained on the ImageNet dataset is then fine-tuned using the labelled wheat patches.

Figure 1 Examples of patches classified as "headed" (top row) and "not headed" (bottom row).

[1] www.hiphen-plant.com/our-solutions/iot-field-sensor

Table 1 Number of labelled patches used to train, validate and test the CNN to detect the presence of ears. The images in the test group belonged to different varieties than those used in the training and hyper-parameter tuning.

	Headed	**Not-headed**
Training	3676	3775
Hyper-parameter tuning	1008	1008
Test	1255	1255
Total patches	**5939**	**6038**

Pretraining combined with data augmentation is an efficient strategy to improve the convergence and regularization of CNNs when the volume and the variability of available images of the training dataset are limited as in our case.

Classification performance of the CNN was evaluated based on three metrics:

a) Overall accuracy $OA = \frac{T_p+T_n}{N}$ *b)*Precision $P = \frac{T_p}{T_p+F_p}$

*c)*Recall $R = \frac{T_p}{T_p+F_n}$

where T_p and T_n are true positive and true negative; F_p and F_n are false positive and false negative respectively; and N is the total number of patches.

2.4 Estimation of the heading date: The expert criteria to determine visually the heading date (Section 2.2) was transposed to identify automatically the heading date from the analysis of classified patches: the proportion of plants with at least 50% of ears emerged is approximated by the fraction $f_{head}(d)$ of patches classified as "headed" belonging to an image taken on date d. Therefore, heading date, d_{head}, is defined when $f_{head}(d_{head}) = 0.5$ (Figure 2).

3 Results and Discussion

3.1 CNN's ability in recognizing ears in patches: The fine-tuned CNN shows an overall accuracy of 95.2% on the test dataset with a recall of 90.6%. The false positives are very marginal (precision is 99.7%) and mainly linked with quality issues of the patches (rain, blur), inducing wrong ear detection.

3.2 Accuracy of the heading date estimation: The graph in Figure 3 shows the performance of the method compared to the visually determined reference date in the 21 fields not used in the training of the CNN. The automatic method can detect the heading date with an average error of 1.58 days over most of the plots. The outlier circled in red had a maximum error of 8 days delay. On inspection, it was found that it corresponds to a plot with zero nitrogen fertilization experiments and was difficult to deduce the presence of wheat ears by visual interpretation of the images.

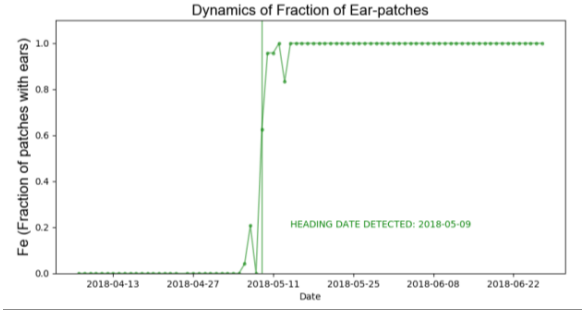

Figure 2 Determination of heading date from the dynamics of $f_{e,d}$

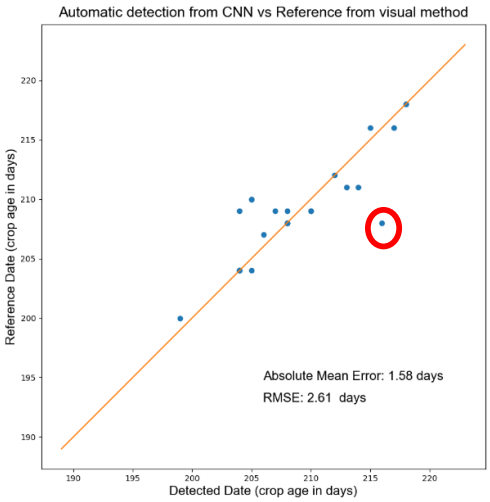

Figure 3 Comparing the wheat heading date estimated by the model with reference dates in the 2017 and 2018 campaigns.

4 Conclusion

Thus, through this study we have developed a simple method which is robust over wheat varieties in detecting the heading stage with an average error of 1.5 days. Further study is needed to improve the classification performance and understand why it fails to recognize ears in some cases. Another suggestion is to use a count-based method to identify the heading date to accurately identify the day where 50% of the ears have emerged within the sampling area.

References

[1] H. Yalcin, "Phenology recognition using deep learning: DeepPheno," *26th IEEE Signal Process. Commun. Appl. Conf. SIU 2018*, pp. 1–4, 2018.

[2] J. C. Zadoks, T. T. Chang, and C. F. Konzak, "A Decimal Code for the Growth Stages of Cereals.," *Weed Res.*, vol. 14, no. 6, p. 415–421., 1974.

[3] C. Szegedy, S. Ioffe, V. Vanhoucke, and A. Alemi, "Inception-v4, Inception-ResNet and the Impact of Residual Connections on Learning," Feb. 2016.

Phenomobile: a fully automatic robot for high-throughput field phenotyping of a large range of crops with active measurements

Frédéric Baret[1], Benoit de Solan[2], Samuel Thomas[2], Philippe Burger[3], Shouyang Liu[1], Alexis Comar, Christophe Rousset[4], Robin Vanhove[4], Romain Regnier[4], Jerome Terreni[5] and Laurent Combe[5]

[1] INRA UMR 1114 EMMAH, UMT CAPTE, F-84914 Avignon, France
[2] Arvalis, UMT CAPTE, F-84914 Avignon, France
[1] INRA UMR 1248 AGIR, F-31326 Castanet Tolosan, France
[3] HIPHEN, UMT CAPTE, Domaine Saint-Paul, Site Agroparc, F-84914 Avignon, France
[4]Robopec, F-83140 Six-Fours-les-Plages, France
[5]Meca3D, F-84100 Carpentras, France

Abstract

High-throughput phenotyping data acquisition in the field is highly required to provide breeders with a set of accurate and heritable traits for the evaluation of the genotypes performances. An entirely automatic robot was developed, called Phenomobile, able to sample with a 100-200 plots/hour throughput using a 12m long telescopic arm moving from 1m to 4m height. The vehicle is mounted on caterpillars to operate under difficult soil conditions. The measurement heads include LiDARS, high resolution RGB cameras and multispectral cameras used in active mode with flashes. The phenomobile is driven by RTK-GPS with centimetric accuracy. Sensors are automatically triggered according to a predefined mission, and the data stored under standard format for easy processing. Fist results and conclusions are given in this paper.

Keywords: Field phenotyping, Remote Sensing, Robot, Unmanned Ground Vehicle.

1 Introduction

Acquisition of phenotyping data in field conditions is mandatory to support breeders with pertinent information on the performances of the genotypes. Although UAVs allow to characterize the genotypes with a number of traits, their application is often limited to some of the traits requiring either very high resolution imagery, high power consumption or heavy payload sensors. Further, UAV observations are mainly completed in passive mode, making the measurements sensitive to the illumination conditions prevailing during the data acquisition. Finally, flying UAVs might be limited by local regulations. Although associated with a lower throughput, Unmanned Ground Vehicles (UGV) is a versatile solution that carries a number of sensors operating in active mode from very low distance to the canopy allowing to record very high spatial resolution images. This paper presents a UGV called Phenomobile, that was specifically developed to sample a range of crops including tall crops such as sunflower or maize and crops that fills rapidly the interval left between two consecutive plots such as rapeseed or peas.

2 Description of the phenomobile

The phenomobile is made of three main components: (1) the vehicle, (2) the measurement head and (3) the data acquisition system.

a. The vehicle

The platform weigh eight tons (Figure 1). It is equipped with four caterpillars allowing to operate even under difficult soil conditions with limited damage. The platform can rotate 360° along a vertical axis above the caterpillars. It supports the diesel engine with 8 hours autonomy that runs both the hydraulic and electric units. The 12 m telescopic boom can raise the measurement head from 1 to 4 m height. A cockpit allows an operator to ensure the security when the regulations do not authorize a full autonomous driving. The vehicle is running on the alleys, making stops on specific positions to sample a group of 1 to 12 microplots on both sides of the alley. The throughput is in between 100-200 plots per hour depending on the plot size.

Figure 1. The phenomobile with caterpillars showing the 12m long boom supporting the measurement head.

b. The measurement head

The measurement head (Figure 2) is made of two units: one looking vertically, the other looking at a given incidence angle from the side. The two units are positioned to sample approximately the same crop volume. Each unit is equipped with LiDARS, high resolution RGB cameras and multispectral cameras. The cameras are operated in active mode using powerful flashes, making the measurements fully independent from the illumination conditions.

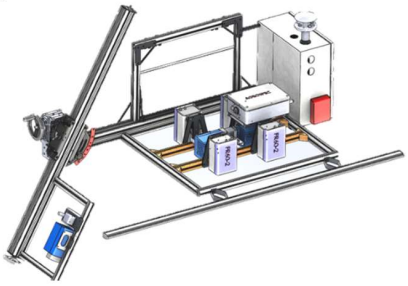

Figure 2. The measurement head with its vertical and side units. Each unit includes LiDARS (in blue), RGB and multispectral cameras operated with flashes. The white box on the right hosts the acquisition system.

c. The data acquisition system

The acquisition system is run by a PC using the ROS operating system dedicated to robotics. The acquisition system triggers the measurements that are then recorded in HDF5 format along with all the metainformation required to ensure FAIR principles in data management, including position and time stamp. The system is driven by phenoIHM (Figure 3), the application that defines and runs the mission.

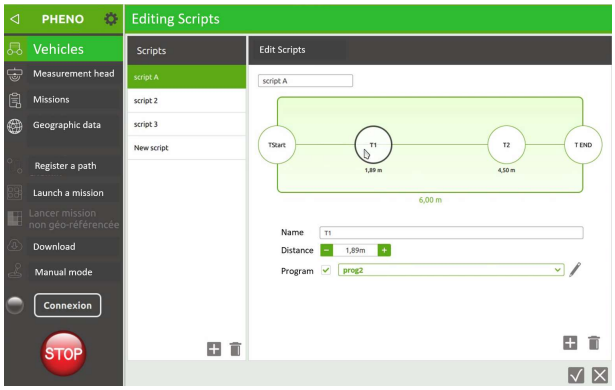

Figure 3. One typical page of the "phenoIHM" interface used to define a script for a given microplot.

A mission corresponds to a measurement session, i.e. the sampling of a group of plots completed at a given date/stage along the growth cycle. It is therefore necessary to define the vehicle and measurement head used, with all the settings of the sensors. The trajectory (path) of the vehicle is then defined, with the several stops required to sample the plots considered. Then the script that describes the set of measurements to make on a given plot is defined by the start and stop positions (beginning and end of the plot) and all the positions where images are shot (Figure 3). Several tools help to define the mission by automatically repeating a script for a large number of plots. Once a mission is defined, it can be run automatically up to its completion. Warnings and a log file allows to control the quality of the measurements both in real time and after the mission ended.

3 Sample results and conclusion

The phenomobile started to operate in 2017 in Toulouse and two more copies are currently operating in Clermont and Montpellier. First results indicate a very good accuracy (Figure 3) due to the high spatial resolution available and the independency from the illumination conditions. Further, a very high repeatability (Figure 3) is also achieved allowing to get high values of heritability (Figure 4) and very good time consistency.

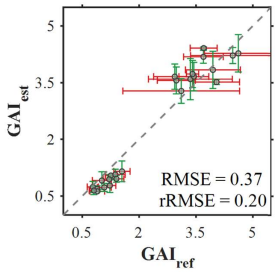

Figure 3. Comparison of phenomobile derived GAI trait as compared to reference ground measurements. Data from Greoux experiment on wheat conducted in 2018.

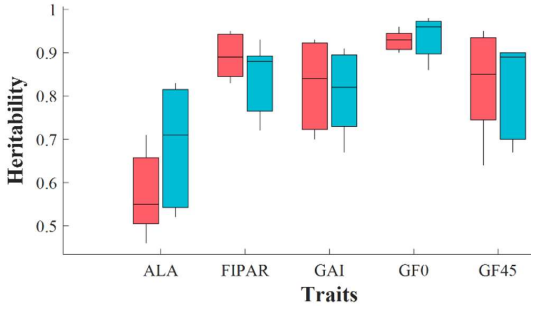

Figure 4. Heritability levels reached for several structural traits (Average Leaf Angle (ALA), Fraction of light intercepted (FIPAR), Green area index (GAI) and green fractions at 0° (GF0) and 45°(GF45)) derived from the Phenomobile over a wheat experiment in 2018 in Gréoux with well-watered (red) and water-stress modalities.

It is concluded that the phenomobile is a very efficient system for a detailed monitoring of structural traits. It is further possible to easily add sensors to access new traits, particularly those benefiting from active measurements difficult to make from a UAV platform.

Acknowledgements. This study was supported by "Programme d'investissement d'Avenir" PHENOME (ANR-11-INBS-012)

Hierarchical structure of tree leaf veins

Aurélie Leborgne[1], Julien Mille[2], and Laure Tougne[3]

[1]Université de Strasbourg, iCube (UMR 7537), CNRS, Illkirch, France
[2]INSA Centre-Val de Loire, LIFAT (EA 6300), Blois, France
[3]Université Lyon 2, LIRIS (UMR 5205), CNRS, Lyon, France

Abstract

Leaf veins make hierarchical networks. According to botanists, the mechanisms of their formation come from the minimization of mechanical constraints. So, the vein network of a given leaf is an important characteristic to know the species of that leaf. We present an automatic algorithm to extract and hierarchize the network of leaf veins in order to use it in various studies, such as comparison between species. The input to our method is a single photograph, taken by a smart-phone in a natural environment. From an initial binary segmentation of veins, we use a thinning algorithm and a recursive labelling method to extract the hierarchical structure, stored in a hierarchical hypergraph.

Keywords: Leaf venation architecture, segmentation, hypergraph.

1 Introduction

Leaf venation is the result of a complex development. In this paper, we focused our work on tree leaves, which are part of *dicotyledonous* plants. First of all, notice that these leaves share a common structure framework and developmental algorithm [7]. Indeed, plants grow according to a hierarchy based on vein diameter and branching. This hierarchy is very important. It allows, in particular, to optimize the transport of water so that leaves feed as easily as possible [3, 6]. Typically, in a leaf, there are one or more first order veins, called *major veins*. These veins run from the petiole towards the leaf apex. They can be compared to the main trunk, or trunks, of a tree. *Second (2°) order veins* are branching off on a major vein. They are analogous to the major limbs of a tree [1]. *Third (3°) order veins* are branching off on a second order vein. There also are *minor veins* forming a mesh between veins of higher order. The general hierarchy of leaves veins is presented on an example in Figure 1.

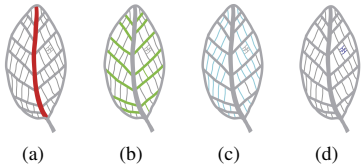

Figure 1: Hierarchy of leaf veins [7]. (a) Major vein (red), (b) 2°order veins (green), (c) 3°order veins (light blue), (d) minor veins (dark blue).

2 Our contributions

Previously, we worked on an automatic extraction of leaf network of veins [5] basing our proposition on the *medialness* measure [4], which allows to extract tubular structures. Some examples are presented in Figure 2.

Figure 2: Examples of automatic extraction of leaf network of veins [5].

In this paper, we present the next step: a method, which allows to obtain a hierarchy in the most basic venations of leaf (pinnate and palmate are presented in Figure 3). More specifically, we are interested in the primary and secondary veins, which are the major structural veins of leaf [1].

First of all, we thin the segmented veins while preserving their topology, in order to represent veins in a concise way. To do that, we used the MB2 algorithm [2]. This parallel algorithm allows to obtain a set of connected curves having a thickness of one or two pixels. To obtain a curve having exactly one pixel of thickness, a post-processing is added. We remove all the single points (that do not disconnect the curve), which are not terminal (that have more than one one neighbor in leaf veins) thanks to the Yokoi criterion [9].

(a) Pinnate (b) Palmate

Figure 3: Most basic venations of leaf [8].

To obtain a hierarchy of leaf veins, we make assumptions based on botanical literature. In pinnate and palmate, primary and secondary veins are almost rectilinear. They run from the base of the leaf toward the margin [1].

Based on such assumptions, we developed a recursive algorithm taking as input the previously segmented leaf veins and the beginning area (area already hierarchized). At the first iteration of the algorithm, this area is the base of the leaf. The hierarchy level is the label that we want to assign to the corresponding veins. This algorithm returns Results, all veins labelled by the level of hierarchy from the beginning area. At the beginning, Results is initialised to empty set. In this algorithm, we use the notion of branch, which is a sequence of pixels connecting either two intersection points or, an intersection point and an endpoint.

Algorithm 1 Hierarchy of leaf veins

```
1:  function HIERARCHY(veins V, beginning area A, level of hierarchy L)
2:      for each branch from A do
3:          - Among all the paths beginning at A
4:          and leading to the margin of the leaf,
5:          keep path P the most rectilinear as possible
6:          based on the angles
7:          - Label P with L
8:          - Add P to Results
9:          if L ≤ 1 then
10:             Results ← Results+hierarchy(V,P,L+1)
        return Results
```

Some examples of results are shown in Figure 4 where pixels belonging to major veins are automatically colored in red and pixels belonging to second order veins in yellow.

3 Conclusion and futur works

To conclude, we extracted and hierarchized the veins of the majority of the tree leaves. To continue this work, we will take into account the diameter of the veins, in order to be in agreement with the observations of the biologists [7]. So that our method can be applied to all plant species. Finally, we will use these results in order to recognize the plant species from a photo of one of their leaves.

Figure 4: Examples of hierarchy of leaf vein.

Acknowledgment

We thank Gravegeal Dorian, Ushaka Kubwawe Kevin, Fournier Dorian and Pons Yuri for their work in this project.

References

[1] A Ash. *Manual of leaf architecture: morphological description and categorization of dicotyledonous and net-veined monocotyledonous angiosperms*. 1999.

[2] TM Bernard and A Manzanera. Improved low complexity fully parallel thinning algorithm. In *IEEE ICIAP*, pages 215–220, 1999.

[3] H Cochard, F Froux, S Mayr, and C Coutand. Xylem wall collapse in water-stressed pine needles. *Plant Physiology*, 134(1):401–408, 2004.

[4] AF Frangi, WJ Niessen, KL Vincken, and MA Viergever. Multiscale vessel enhancement filtering. In *MICCAI*, pages 130–137, 1998.

[5] A Leborgne, J Mille, and L Tougne. Automatic extraction of leaf network of veins. In *IAMPS*, 2018.

[6] Athena D McKown, H Cochard, and L Sack. Decoding leaf hydraulics with a spatially explicit model: principles of venation architecture and implications for its evolution. *The American Naturalist*, 175(4):447–460, 2010.

[7] L Sack, C Scoffoni, AD McKown, K Frole, M Rawls, JC Havran, H Tran, and T Tran. Developmentally based scaling of leaf venation architecture explains global ecological patterns. *Nature Communications*, 3:837, 2012.

[8] R L Walls. Angiosperm leaf vein patterns are linked to leaf functions in a global-scale data set. *American journal of botany*, 98(2):244–253, 2011.

[9] S Yokoi, J-I Toriwaki, and T Fukumura. An analysis of topological properties of digitized binary pictures using local features. *CGIP*, 4(1):63–73, 1975.

A strategy for multimodal canopy images registration

Clément Douarre[1,2,3], Carlos F. Crispim-Junior[1], Anthony Gelibert[3], Laure Tougne[1], and David Rousseau[2]

[1]Univ Lyon, Université Lyon 2, LIRIS, UMR CNRS 5205, F-69676, Lyon, France
[2]Laris, UMR INRA IRHS, Université d'Angers, 62 Avenue Notre Dame du Lac, 49000 Angers, France
[3]Carbon Bee, Rue du Commerce, ZA Les Plaines, 26320 St Marcel-Lès-Valence, France

Abstract

Registration of complex and self-similar images such as plant canopy images is a challenge in plant sciences. Yet, this is often a required step for multimodal imaging, where unaligned sensors yield unregistered image pairs. We propose a pipeline adapted to such constraints, applied to apple tree canopies. Specifically, we apply an intensity-based registration on downscaled and/or Gaussian blurred versions of the targeted images. This helps to eliminate spurious details, which smooths the optimization landscape and also helps to reduce differences between the modalities. Results show better registration than with standard feature-based or intensity-based methods.

Keywords: Registration, Multimodal Imaging, Apple scab, Infrared Imagery.

1 Case study

Apple scab is one of the most serious fungal infections of the apple tree. RGB imaging has shown success for automatic scab detection [2], but to improve its treatment, early detection, *i.e.* before visible symptoms, would be valuable. Infrared (IR) imagery has been shown to be suitable for this task [1].

Our goal is to perform automatic detection of scab on apple plants images acquired both in RGB and in IR. We acquired such multimodal images of apple plants inoculated with scab, from a canopy point of view. Acquisition was done in the LARIS laboratory (Angers) greenhouses in the 2018-19 period. The sensor was a multimodal camera developed by the company Carbon Bee. However, like in many multimodal acquisitions cases, RGB and IR sensors were not exactly aligned and thus, the two modalities of a given acquisition were shifted (Fig. 1).

Figure 1: An example of a RGB (left) and a IR (right) image pair. A yellow rectangle is drawn on both images at the same position. This shows the offset, which seems a feasible objective for a registration algorithm.

This offset was an important problem for us as we needed the images to be aligned for the rest of our analysis to work. Therefore, we needed to perform registration within image pairs.

2 State of the art

Image registration techniques may be grouped in two families [6]: feature-based and intensity-based.

Feature-based methods use matching features in image pairs to find the transformation. The most well-known features are SIFT [4]. However, even with careful tuning of the SIFT algorithm, we find that our images are not suitable for this kind of registration. We can see in Fig. 2 that keypoints in one modality are numerous and incorrectly matched with keypoints in the other, and that there are almost no correct matches. The facts that (i) there are highly complex and self-similar structures in our images, and (ii) leaves have a different aspect depending on the modality, make these images a bad fit for such a registration.

Figure 2: Keypoints found by SIFT and the 20 strongest matches on an image pair, drawn as black lines.

Intensity-based methods consist in warping one image while keeping the other fixed, guided by the optimization of some similarity metric between the two images. This kind of registration applied to multimodal grapevine canopies has been done by *e.g.* [5]. Our method is an adaptation of such a registration, adapted to the specificities of our images.

3 Method

To perform an intensity-based registration, one must choose the warp type and the similarity metric. Since the images represent the same scene acquired through two cameras, the transformation between the images resembles a homography (it is not exactly so, as the scene is non-planar: leaves are at different heights in the canopy). Accordingly, the warping was set to a homography rigid transform. Concerning the similarity metric, we chose the Enchanced Correlation Coefficient (ECC) [3]. It is a measure of similarity between normalized images ($ECC \in [0, 1]$). Hence, it can interestingly, like Mutual Information, work with multimodal images.

Having checked visually that a high ECC between two images correlates with an adequate registration, we used this metric to assess registration quality. Our first registration attempts using ECC were sometimes quite poor: We hypothesized that this was because of the numerous details in the scene, yielding a highly non convex similarity metric optimization landscape.

Consequently, the contributions of this paper are the following modifications on the intensity-based registration: perform the registration on images whose resolution are lowered, through downscaling and/or Gaussian blur.

4 Results

We applied our method to a dataset composed of 50 image pairs of 2592×1944 pixels. Image pairs were acquired at different times and orientations, leading to a relatively diverse dataset (Fig. 3). In particular, the offset between images varied from pair to pair. For each image pair, we applied the same downscaling/blur transformations to the two images, registered those images, and adapted the resulting registration homography matrix back to the original images.

Figure 3: Examples of RGB images from the dataset.

When using SIFT, registrations did not improve ECC for any of the image pairs in the dataset. With the proposed strategy, a combination of strong downscale and a strong blur yielded the best results (Table 1, Fig. 4). Those were the cases where some details were "blurred out" and where the only remaining high frequencies were ones from leaf borders, which are robust features for such a multimodal registration. The details blurred out could even be misleading: inner structures in IR images could strongly differ from the ones in RGB (*e.g.* scab vs veins) while leaf contours stayed similar. In other words, our strategy enabled us to control the scales our registration worked at.

	$\sigma = 0$	$\sigma = 2$	$\sigma = 4$	SIFT
$d = 1$	8.4	9.4	10.0	0.0
$d = 0.5$	9.4	10.5	10.8	0.0
$d = 0.1$	10.9	11.5	12.0	0.0

Table 1: Results of our registration method on our database : difference of ECC (in %) between the registered pair of images and the original pair, averaged over all pairs in the dataset. d refers to the scale applied to each dimension of the images. σ refers to the Gaussian blur s.d. The last column refers to registration done by SIFT with different d values.

Figure 4: An example of registration from a pair of our dataset, with $d = 0.1$ and Gaussian blur, $\sigma = 4$.

5 Perspectives

Further work will focus on multiple resolution registration: once images have been registered at a lower resolution, perform another registration at a higher level of detail, starting from the first registration. Once the registration will satisfy us, we will pursue our analysis of automatic scab detection, taking full advantage of both modalities.

References

[1] É. Belin et al. Thermography versus chlorophyll fluorescence imaging for detection and quantification of apple scab. *AGR*, 90:159–163, 2013.

[2] S. Delalieux et al. Hyperspectral indices to diagnose leaf biotic stress of apple plants, considering leaf phenology. *IJRS*, 30(8):1887–1912, 2009.

[3] G. Evangelidis et al. Parametric image alignment using enhanced correlation coefficient maximization. *TPAMI*, 30(10):1858–1865, 2008.

[4] D. Lowe. Object recognition from local scale-invariant features. In *ICCV*, pages 1150–1157. Ieee, 1999.

[5] X. Wang et al. Efficient registration of optical and ir images for automatic plant water stress assessment. *AGR*, 74(2):230–237, 2010.

[6] B. Zitova et al. Image registration methods: a survey. *IVC*, 21(11):977–1000, 2003.

Toward an automatic Bean Rust disease quantification platform using hyperspectral sensing and Deep Learning

Anthony Gelibert[1], Aurélie Thébault[2], Laurent Descroix[3], Erica Manesso[4], Catherine Sirven[3]

[1]Carbon Bee, Z.A. Les Plaines, Saint Marcel les Valence, France
[2]Carbon Bee AgTech, Z.A. Les Plaines, Saint Marcel les Valence, France
[3]Bayer, La Dargoire, Lyon, France
[4]Bayer, Hoechst Industry Park, Frankfurt, Germany

Abstract

Automatic disease quantification on whole plants is a complex human process and lacks, to our knowledge, turnkey solutions for controlled conditions screening processes. By using a custom phenotyping platform based on a hyperspectral sensor and Deep Learning algorithm, we built the first step toward a fully integrated automatic Bean Rust disease quantification in controlled conditions.

Keywords: Plant Sciences, Hyperspectral, Deep Learning, Remote Sensing, Bean Rust

1 Introduction

To discover new active chemical molecules against plant diseases, several steps of compound screening are performed in the early research phases. Only about 1 molecule over 160,000 will succeed in reaching the agrochemical market, and only after about 12 years of research and development activities, including efficiency testing, optimization cycles and environmental/human safety. This process implies the activity testing of small molecules on diseased plants at a high screening throughput. For example, about 3,000 bean rust plants, aged around 2 weeks, are visually assessed by humans every week in order to detect active compounds against bean rust (*Uromyces appendiculatus*). The automation of these tasks would be of great interest to enhance the screening process and reduce variability within and between ratings [1, 2].

However, the task of disease quantification on a whole plant is a complex human process [3], not easily done with image analysis and automatism, even if the literature shows an interest in these technologies [4]. Moreover, the solution has to maintain a "compatibility" (correlation) with all the previous data obtained by manual assessment even if quantification from human vision and pixel counting will be different.

In this contribution, we will present our first steps toward a fully automated disease quantification platform based on a hyperspectral sensor and an Artificial Intelligence (supervised Deep Learning [5, 6]). The gap between human and machine results is reduced by post-processing.

2 Methods: dataset

To obtain the training dataset, we built an *ad hoc* phenotyping platform including an AQiT-Sensor[1] (full spectrum between 300 and 1000 nm) under LED lighting (Fig. 1). The data were produced from 380 real plants displaying gradient of infection related to disease severity from 0 to 100%. The plant reflectance was captured from the top with leaves placed in a flat configuration (Fig. 2).

The disease was rated twice: *in situ* (i.e. simultaneously to image capture) on whole plants by a human assessor (ground truth), as well as on pictures independently by 4 different human assessors. Then, a manual annotation of the disease was done over 120 pictures to perform the learning phase of Deep Learning (DL) algorithm.

3 Methods: processing

Once the dataset was produced, the images were post-processed to train the Artificial Neural Network [5].

To focus on the AI (Artificial Intelligence) processing on the leaves, pictures were segmented by computer vision to remove the specific blue background color of the phenotyping platform (Fig. 1). A SegNet-like encoder-decoder

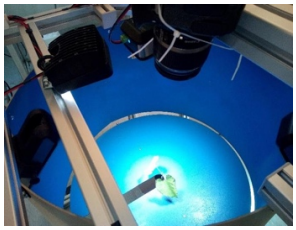

Figure 1: Phenotyping platform

[1] https://carbonbee.fr/images/agrotech/Datasheet-AQiT-Sensor-FR.pdf

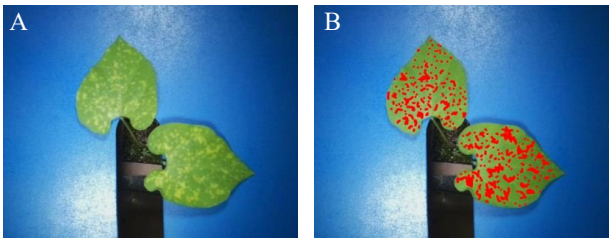

Figure 2: Example of rust infected bean plant picture (A) and annotated picture (B). Red coloration is used to highlight the plant diseased area.

segmentation neural network was used to segment disease symptoms [6]. Initial weights were randomly set by AI.

The training process follows state-of-the-art guidelines for AI training, including balanced MSE cost function, Adam back-propagating, F1-scoring and 70/30% ratio between training/test data.

First, visual assessment of AI detection was performed on a subset of 30 non-annotated plants. In a second step, estimations of infected surface detected by AI were compared to human annotations for all 380 rated plants.

4 Results

The segmentation of bean rust symptoms on bean leaves was relevant (Fig. 3). At the pixel scale, F1-score reached 71 %. Even if the detected symptoms surface was often lower than the human assessment (especially in the 40-60 % severity range), the evaluation proved more consistent over the whole severity gradient.

Interestingly enough, AI did not confuse rust bean symptoms with other symptoms, such as clearer veins or discoloration zones. The comparison of detected surface and visual observation showed high linear correlation, with a mean root square error below 10%, which was within the range of human error (Fig. 4).

5 Future Works

This publication is the first step towards a fully integrated platform for an automated disease surface measurement. The evaluation showed the relevance and feasibility of the analysis, as the AI was able to clearly spot the symptoms of the rust without falling into the trap of similarities.

On the other hand, there remains some scientific locks to tackle.

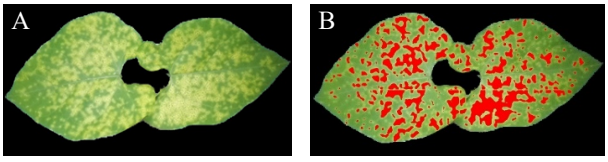

Figure 3: Example of rust infected bean plant picture (A) and AI detection (B) on highly infected leaves.

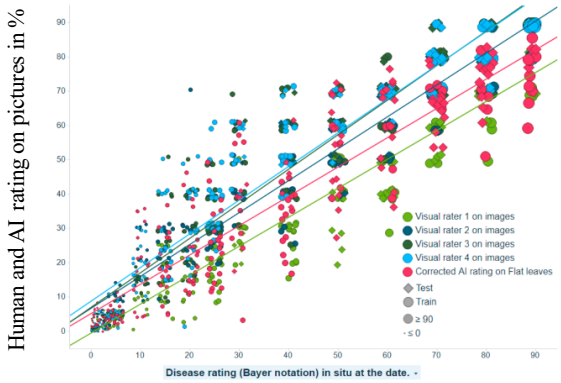

Figure 4: Disease quantification (in %) obtained from comparative disease rating between human and AI. Reference is *in situ* evaluation.

AI evaluations were systematically different (but correlated) from those of humans and a reliable and robust non-linear adjustment function remains to be built.

Moreover, some mechanical aspects of the platform need to be corrected in order to stabilize and improve the spectrum quality (especially in the near IR).

Acknowledgement

Plant production, image collection and annotation were performed by Yannick Tarriotte, David Chambouvet and Kelly Bonnel. Carbon Bee gratefully thanks Amélie Achard, Arthur Jeanselme, Gérald Germain, Nathanaël Spriet and Nicolas Hilaire. The study was financed by Carsten Beyer in the computational Life Science Portfolio group in Monheim. We thank Steffen Vogler for pertinent advices.

References

[1] Godoy, C. V., Koga, L. J., & Canteri, M. G. (2006). Diagrammatic scale for assessment of soybean rust severity. *Fitopatologia Brasileira*, *31*(1), 63–68.

[2] Parker, S. R., Shaw, M. W., & Royle, D. J. (1995). The reliability of visual estimates of disease severity on cereal leaves. *Plant Pathology, 44*(5), 856–864.

[3] Clive, J. W. (1971). An illustrated series of assessment keys for plant diseases, their preparation and usage. *Edit. WL Seaman. Can. Plant Dis. Surv*, *51*, 2.

[4] Mahlein, A. K., Oerke, E. C., Steiner, U., & Dehne, H. W. (2012). Recent advances in sensing plant diseases for precision crop protection. *European Journal of Plant Pathology*, *133*(1), 197–209.

[5] LeCun, Y., Bengio, Y., & Hinton, G. (2015). Deep learning. *Nature*, *521*(7553), 436.

[6] Badrinarayanan, V., Kendall, A., & Cipolla, R. (2017). Segnet: A deep convolutional encoder-decoder architecture for image segmentation. *IEEE transactions on pattern analysis and machine intelligence*, *39*(12), 2481–2495.

7th IAMPS 2019, 4-5 July 2019, Lyon

International Workshop on Image Analysis Methods for the Plant Sciences

Reviewing comitee

Ayadi	Mehdi
Briot	Sébastien
Burguet	Jasmine
Cerutti	Guillaume
Cohen	Julia
Crispim Junior	Carlos Fernando
Douarre	Clément
Kerautret	Bertrand
Lamy	Jonas
Lemaire	Pierre
Miguet	Serge
Misra	Debaleena
Ratajczak	Rémi
Scuturici	Mihaela
Tougne	Laure

Organizing comitee

Ayadi	Mehdi
Cohen	Julia
Crispim Junior	Carlos Fernando
Douarre	Clément
Kerautret	Bertrand
Lamy	Jonas
Lemaire	Pierre
Misra	Debaleena
Ratajczak	Rémi
Tougne	Laure
Villeseche	Catherine